Space and Time Resolved Ion Doppler Temperature and Velocity Measurements in Z-pinch Plasmas on the ZaP-HD Device

Shane Murray

A thesis

submitted in partial fulfillment of the

requirements for the degree of

Master of Science in Aeronautics & Astronautics

University of Washington
2024

Reading Committee:
Uri Shumlak
Justin Little

Program Authorized to Offer Degree:
Aeronautics & Astronautics

University of Washington

Abstract

Space and Time Resolved Ion Doppler Temperature and Velocity Measurements in Z-pinch Plasmas on the ZaP-HD Device

Shane Murray

Chair of the Supervisory Committee:

Uri Shumlak
Department of Aeronautics & Astronautics

The ZaP-HD Flow Z-Pinch device has shown that sheared-flow can stabilize a plasma in a simple Z pinch configuration for times well over that of a static Z pinch. The plasma is stabilized when the shear flow passes the threshold of $\frac{dV_z}{dr} \geq 0.1kV_A$, mitigating the 'kink' instability. The ZaP-HD research project shows promise as both a compact fusion device and as a hypothetical in-space propulsion device. Impurity line radiation from the plasma allows for noninvasive spectroscopic techniques that can provide measurements for various plasma parameters of interest. Time-resolved spectroscopy measurements have been taken on the device in the past, however a new setup with a different high speed camera is used, resulting in measurements with over twice the spatial resolution. Ion Doppler spectroscopy (IDS) is used to measure temperature and velocity of carbon III ions in the plasma. Improved signal due to erosion of the graphite nose cone increases the amount of data collected, allowing for a more complete picture of the pinch behavior over the plasma lifetime. Sheared-flow passing the threshold for stability is found for much of the pulse duration with speeds up to 150 km/s and temperatures up to 500 eV. Time resolved temperature and velocity profiles indicate plasma reflecting off the end wall and propagating upstream as a stagnation wave, causing jump conditions comparable to that of a normal shock in the plasma. An

upper limit of thruster performance is found using IDS data in conjunction with typical plasma parameters to yield an effective thrust of 0.216 N and specific impulse of 5.76×10^4 s.

CONTENTS

LIST OF FIGURES

LIST OF TABLES

ACKNOWLEDGEMENTS

I could not have completed this thesis without the help and support of all the other members of the lab. I would like to extend a special thank you to Aqil Khairi, Jared Smythe, Harry Furey-Soper, Elyse Lian, Bennett Diamond, and Aria Johansen who all played an important role in this thesis, whether it was helping collect data or being available and willing to discuss results with me. I would also like to thank my advisor, Uri Shumlak, for being a willing guide and mentor throughout the past two years. Of course I would not be in this position without my family, who have supported me through my entire lengthy academic journey. A special shout out must also go to Howard Shore, whose score from The Lord of the Rings kept me company on many late nights of writing.

DEDICATION

To my parents. Thank you for everything.

CHAPTER 1

INTRODUCTION

The increasing demand for energy amidst a world growing faster than ever is having a direct toll on the earth. With industrialization and urbanization at all time highs, the human population is using high amounts of energy and releasing massive amounts of greenhouse gases (GHG) as a consequence. CO_2 emissions account for 79% of GHG emissions in the United States and 92% of these CO_2 emissions are due to fossil fuel combustion. Global CO_2 emissions are more than 35 billion tonnes per year [1]. The planet was not made for these amounts of GHGs and the side effects could prove catastrophic for humans and many other life forms living on earth. Climate change effects are already felt today, and without a drastic reduction in GHG emissions soon, they could be irreversible. The race to decrease fossil fuel consumption and thus GHG emissions is the main cause for the surge in renewable energy research. Nuclear fusion energy provides the answer to our planet's biggest crisis with a clean and abundant source of energy.

Our sun and all the stars in the universe are powered by fusion reactions in their cores. Fusion is a naturally occurring phenomenon, but harnessing this power on Earth comes with a slew of complications. If it was easy, fusion would not always be fifty years away. The biggest hurdle for man made fusion devices is confinement. In order to fuse two nuclei, the repulsive Coulomb force must be overcome before the strong nuclear force takes over and holds the nuclei together. The Coulomb barrier two nuclei must overcome varies by $1/r$ and an approximation for the radius of a proton is $\sim 10^{-15}$ m. This leads to an incredibly high energy barrier as the nuclei get closer

together in an attempt to fuse. High energies are needed to overcome this peak and one of the biggest hurdles in terrestrial fusion is confining the high energy particles over time periods long enough for fusion to occur. A minimum value for the density and confinement time of a plasma was developed by Lawson to describe the conditions necessary for fusion reactions to produce energy [2]. The Lawson criterion for a deuterium-tritium (D-T) fusion plasma is:

$$n\tau \geq 10^{14} \frac{s}{cm^3} \tag{1.1}$$

where n is the particle density and τ is the confinement time[Lawson paper]. The criterion depends on temperature as well and the minimum value occurs around a temperature of 20 keV. D-T is a popular choice for terrestrial fusion since it has the largest cross section for reaction, meaning it has the highest probability of actually fusing during a collision. The D-T reaction is given by:

$$D + T \rightarrow \alpha(3.5MeV) + n(14.1MeV) \tag{1.2}$$

α denotes a charged helium particle also called an alpha particle (^4_2He), n is a neutron, D and T are the hydrogen isotopes, deuterium and tritium. Energy is released from this reaction by the mass lost in transforming the reactants into the products and is given by $E = mc^2$. Since c is such a large value, 3×10^8 m/s, even the smallest changes in mass can result in large releases of energy.

Simply causing a fusion reaction is not enough for fusion power to be a feasible solution to the energy problem. The output energy needs to be greater than the input energy. Fusion gain, Q, is the metric used to describe the ratio of fusion power to input power [4]. Breakeven occurs at Q = 1 and is what scientists have been chasing since the dawn of fusion energy development.

$$Q = \frac{P_{out} - P_{in}}{P_{in}} = \frac{P_F}{P_{in}} \tag{1.3}$$

For a magnetically confined fusion plasma that contains charged products, like alpha particles, self

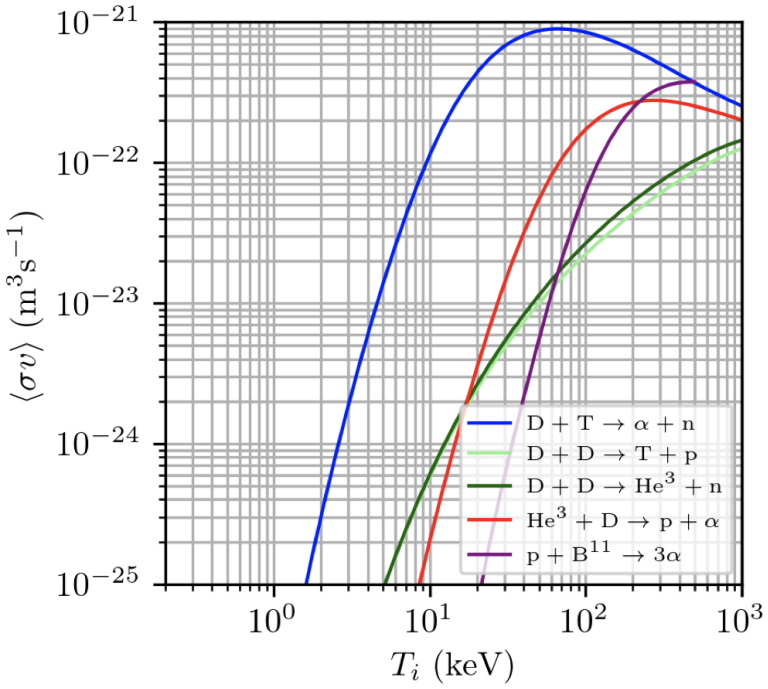

Figure 1.1: Fusion reactivities for common fusion reactions. Can see that the D-T cross section is the highest and peaks at the lowest temperature value [3]

heating from the charged particles that do not escape confinement leads to a new term, Q_{eff}:

$$Q_{eff} = \frac{P_f(1 - f_c)}{P_{in} - f_c P_f} \tag{1.4}$$

with fusion power as P_f, input power as P_{in}, and f_c representing the fraction of energy released by the charged particles. In a sustained plasma, P_{in} must balance power lost. If the power from charged particle heating, $f_c P_f$ balances the input/loss power, the denominator in Q_{eff} trends toward 0 and the effective fusion gain becomes infinite. This process of $Q_{eff} \to \infty$ is called ignition. Reaching the conditions needed for breakeven and eventually ignition come with many challenges. Instabilities, diffusion, and many other loss mechanisms must be mitigated for fusion energy to become a reality [5, Chapter 10].

One of the simplest fusion devices is the Z pinch [6; 7; 8]. The Z pinch started as one of

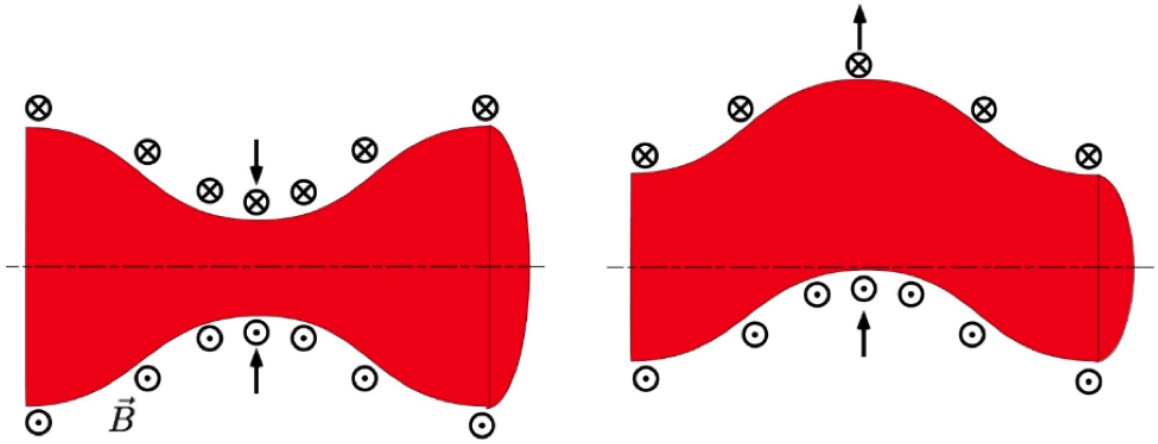

Figure 1.2: Left: m=0 sausage instability is shown with resulting magnetic field strengths. Right: m=1 kink instability is shown with resulting magnetic field strengths

the most promising devices for fusion energy, but was quickly put to the side due to instabilities. Devices like the tokamak, magnetic mirror, and stellarator were more popular due to their stable configurations. In order for the Z pinch to be a viable option, the instabilities needed to be mitigated. The two common magneto-hydrodynamic (MHD) instabilities that affect it are the m=0 mode "sausage" instability and the m=1 mode "kink" instability [9]. In other fusion confinement devices, external magnetic fields help reduce these instabilities. The Z pinch has no external magnetic fields, which reduces the weight and complexity of the device, but makes it more susceptible to instability. Fusion devices must be stable enough to satisfy the Lawson criterion for fusion breakeven. The addition of sheared-flow stabilization (SFS) to the Z pinch configuration allows for a more stable flow and made the it once again a viable option for fusion energy.

Once the problem of fusion energy gain is solved, there are applications for fusion devices beyond energy sources. Interplanetary space missions are held back severely by the current state of propulsion devices. Chemical rockets and electric propulsion systems both have their strengths, but neither has an optimal mix of high thrust and high efficiency needed to make longer space missions realistic. Fusion powered propulsion could provide efficiency beyond the current state-

of-the-art electric propulsion devices along with high thrust for exploration of our solar system and maybe even beyond. The Z pinch is a great candidate for a future fusion space thruster. The plasma in the Z pinch moves axially, so removing the end wall allows for this plasma to propagate outward and produce thrust. Recaptured plasma that does not escape could be used to maintain the plasma current and power the spacecraft. The mass of the thruster would also be minimized compared to other fusion confinement configurations since it has no external magnetic fields. Estimated parameters for a flow-stabilized Z pinch include specific impulse on the order of 10^6 seconds and thrust on the order of 10^5 newtons [10].

1.1 Sheared-Flow Stabilized Z pinch

At its most basic, a Z pinch forms by injecting gas into a vacuum chamber and setting a potential difference between an anode and cathode, which causes an electric field to form between them. This electric field creates a current and, due to Ampere's Law, the current brings about an azimuthal magnetic field. The combination of the axial current and azimuthal magnetic field leads to an inward pointing Lorentz force that pinches the plasma close enough together for fusion to occur. This effect is similar to that seen in the attraction experienced by two parallel wires carrying current in the same direction. The plasma column can be thought of as many current carrying wires in parallel. A static Z pinch will still form a pinch structure, but the MHD instabilities will develop on the order of nanoseconds.

In the static Z pinch, the equilibrium is provided by the inward magnetic pressure $\frac{B_\theta^2}{\mu_0 r}$ balancing the outward plasma pressure.

$$\frac{d}{dr}\left(P + \frac{B_\theta^2}{2\mu_0}\right) + \frac{B_\theta^2}{\mu_0 r} = 0 \tag{1.5}$$

A small decrease in radius increases the magnitude of B and thus the magnetic pressure increases, resulting in a decrease in radius, causing another increase in magnetic pressure, and so on. We can see that even a small perturbation to the pinch radius leads to a runaway destabilizing effect.

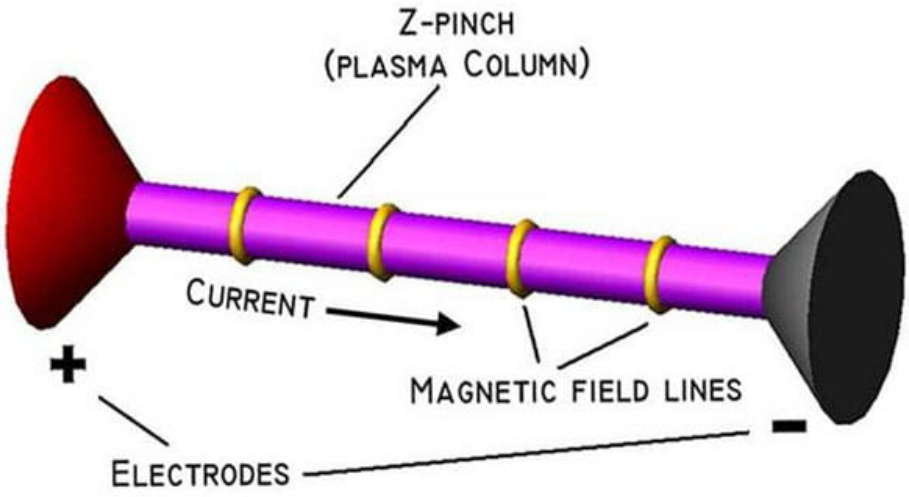

Figure 1.3: A basic Z pinch diagram is shown. Current is seen going from anode to cathode and the resulting azimuthal magnetic field is shown in yellow. The direction of current in this case is ion current.

One way to stabilize the sausage and kink modes that does not limit pressure or temperature of the pinch, like closer walls or an external magnetic field do, is with a sheared-flow. By having faster moving plasma on the outside of the pinch, the plasma is able to quickly fill the gap left by the inward moving edge of a destabilized pinch. A simple analogy is cars on a freeway. If a slow car merges from an outside lane to an inside lane and all the cars are going the same speed, a gap will remain on the outside. However, if the outside lanes are moving faster than the inside lanes, as soon as the slower car merges in, the gap will be filled by the faster moving cars, thus retaining a constant flow on the outside edge and making it harder for any cars inside to merge out. More information regarding the parameters of the sheared flow needed to stabilize sausage and kink modes are provided in Refs. [11] and [12].

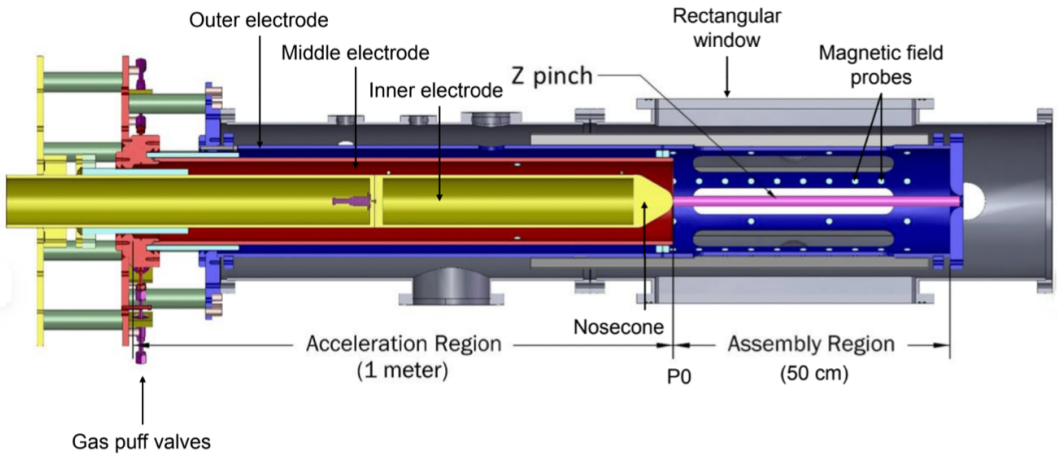

Figure 1.4: CAD drawing of ZaP-HD SFS Z-pinch device

1.2 The Z-Pinch High Energy Density Experiment (ZaP-HD)

The third and most recent iteration of the sheared-flow Z pinch experiment at the University of Washington is the ZaP-HD device. This builds upon the previous two devices, ZaP and FuZE, resulting in a shortened assembly region and the addition of a middle electrode. The shorter assembly region and third electrode increase plasma parameters. The third electrode specifically aims to increase plasma density as more energy can be introduced into the compression region. This increase in energy is achieved by delaying the time between compression and acceleration voltages. A cross section assembly of the device is shown in Fig. 1.3. ZaP-HD uses two capacitor banks as opposed to the one used for ZaP and FuZE to separate the initial ionization and acceleration of the plasma from the second compression stage. A spoked end wall is currently installed in ZaP-HD.

The acceleration capacitor discharges across the inner and middle electrodes. This ionizes the injected neutral gas, which is then accelerated axially due to the $J \times B$ force. Once accelerated into the assembly region a Z pinch will form. After the formation of the pinch, the compression bank

discharges across the inner and outer electrodes, driving the primary plasma current, which further heats and compresses the plasma to higher densities. Fig. 1.4 shows each step of the sheared-

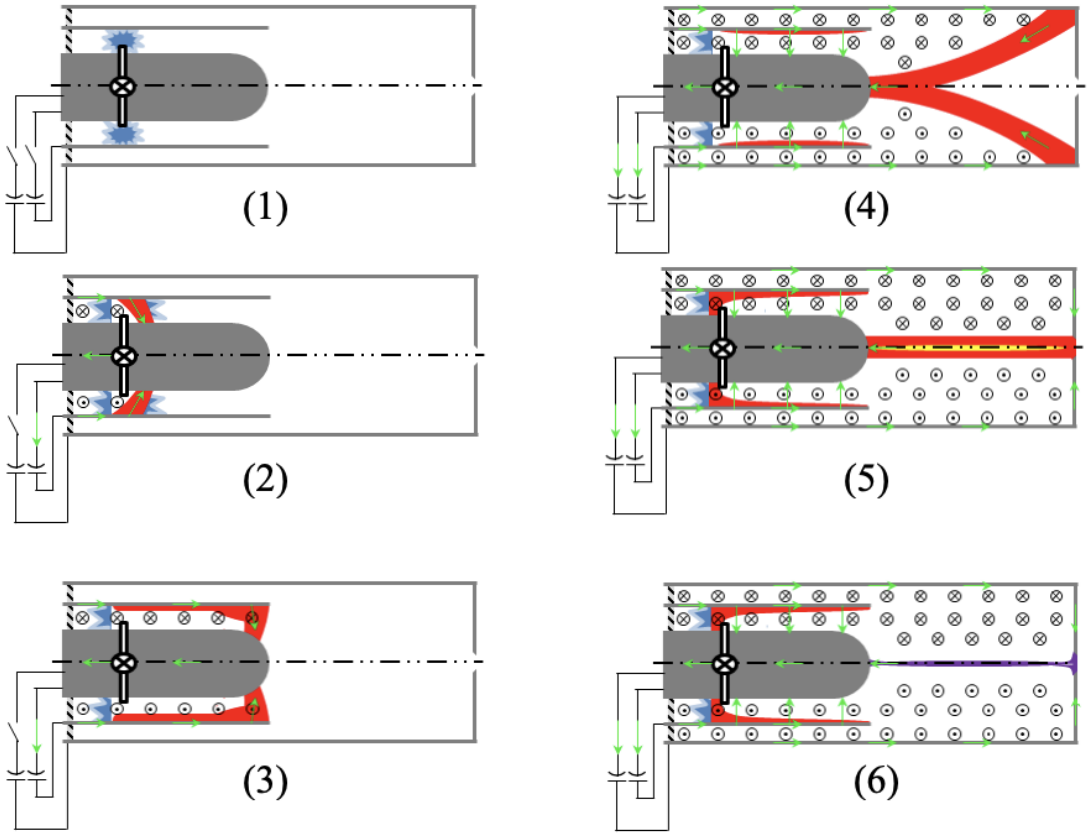

Figure 1.5: Steps in snowplow current evolution. Blue represents neutral gas. Red represents plasma. Purple corresponds to high density plasma. Green arrow shows the electron current

flow formation and second compression stage. Step 1: start of a pulse, neutral hydrogen gas is injected. Step 2: voltage applied between inner and middle electrodes, ionizing gas and creating hydrogen plasma. Step 3: current sheet and subsequent magnetic field accelerate plasma axially due to $J \times B$ force. Steps 4,5,6: once the plasma enters the compression region, a second voltage is applied between the inner and outer electrodes, driving additional current and further compressing

the plasma pinch.

The accelerated current in ZaP-HD operates in a snowplow mode, however, the snowplow mode is not the only current acceleration mode. There are infinite solutions to the conservation equations that govern plasma, however the two most probable are the detonation and deflagration processes. The detonation process leads to the common snowplow model in which a compact current sheet moves axially and ionizes the neutral gas ahead of it. The initial plasma forms and as it accelerates downstream it forms a shock that compresses the neutrals in front of the wave, which are then ionized, leading to compression of the plasma itself and an increase in temperature. The deflagration mode is a more recent discovery and instead of a thin, compact current sheet like the snowplow, a diffuse current conduction region is thought to form in the accelerator region. A stationary upstream ionization zone then continuously ionizes the neutral gas. The initial plasma forms and accelerates due to the Lorentz force and experiences none of the compression and heating associated with the snowplow shock. The magnetic energy is converted mostly into particle motion instead, so the deflagration mode can lead to cooler, higher velocity plasma [13]. In practice a plasma accelerator does not need to operate in one mode or the other. In fact many devices undergo mode transitions during a single discharge. ZaP-HD ideally operates in a mode transition starting with snowplow to ionize and accelerate neutrals in the chamber, creating a plasma in the assembly region, which is then ready to be compressed by the discharge of the compression banks. Now that there are no longer neutrals in the vacuum chamber, the deflagration mode starts, efficiently accelerating the plasma to supply sheared-flow for extended stability.

1.3 Goals and Approach

The objective of this thesis is to determine plasma parameters and pinch behavior both in the assembly region and downstream through the end wall. It aims to build off of previous work investigating the downstream behavior and thruster performance. Former work examined plume characteristics

and thruster performance of ZaP-HD and found that with the end wall off a hypothetical thruster would have a thrust of 123 millinewtons if pulsed at 10 hertz and a specific impulse of 16,000 seconds [14]. In order to improve upon these results and validate them further, I aim to both spatially and temporally resolve plasma parameters. Using a high speed Phantom T2410 camera and image intensifier attached to a spectrometer, ion Doppler spectroscopy (IDS) is used to find the speed of the ions in the plasma. IDS is also used to find ion temperatures in the plasma. Earlier approaches of characterizing the plasma temperature and velocity using an intensified charge-coupled device were limited to one spatially resolved measurement per plasma pulse. For this thesis, measurements are made using a multi-frame high speed camera, allowing for multiple frames of spectra per single pulse. This allows the full time evolution of the temperature and velocity of the pinch to be seen without having to take hundreds of pulses at differing acquisition times. Having a time evolving set of velocity and temperature profiles for each pulse shows a more complete picture of the evolution of the Z pinch and allows for a deeper analysis of the sheared-flow and thruster performance. Previous work on the device used a Kirana high speed camera to characterize plasma parameters over the plasma lifetime, but due to low impurity ion intensity, the data was sparse and mainly limited to the second half of the pinch lifetime [15; 16; 17]. The more recent replacement of the original ZaP-HD nose cone with a graphite version has increased the amount of carbon present in the machine. This paired with the higher resolution and higher light sensitivity of the Phantom increases the amount of data collected per pulse.

CHAPTER 2

ZAP-HD DIAGNOSTICS

2.1 Obtaining Plasma Properties Using Spectroscopic Measurements

Spectroscopy is a well established diagnostic in the field of plasma physics. It owes a lot of its advancement to the fields of chemistry and astronomy and continues to be one of the most used diagnostic tools for many fields. For plasma physics, spectroscopy offers the benefit of being a non-intrusive tool. Plasma emit many forms of radiation including bremmstrahlung, cyclotron, and line radiation that each allow for different insights into the plasma, such as temperature, density, or power losses. As a non-intrusive diagnostic, spectroscopy allows for the measurements of radiation emitted from the plasma without affecting the plasma itself. The radiation of importance for this thesis is line radiation. A carbon impurity in the plasma is examined based on its known line radiation to provide details about the plasma's ion temperature and velocity.

Line radiation is emitted when a bound electron transitions to a lower energy state. The Bohr model of the atom describes a positively charged nucleus orbited by electrons in distinct shells, subshells, and orbitals depending on their quantum numbers. When one of these electrons becomes 'excited', it moves to an orbital in a higher energy level. Electron excitation is usually due to absorption of a photon, photoexcitation, or a collision with a high energy electron, collisional

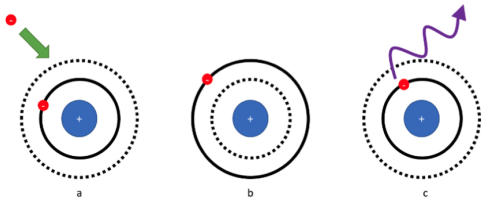

Figure 2.1: a. Excitation event. A free electron with high energy interacts with a relaxed bound electron. b. The relaxed electron is now 'excited' and moves up to a higher energy level. c: The excited electron relaxes, giving off a photon with energy corresponding to the change in energy levels [16]

excitation. Eventually the excited electron will transit from its higher energy level to a lower one through spontaneous emission. When the electron relaxes, it releases a photon with energy equivalent to the change in energy from the higher energy level to the lower. The wavelength of the emitted photon is unique to the transition and depends on the specific ion and orbitals involved. The wavelength is described by the following relation:

$$\Delta E = \hbar/\lambda \tag{2.1}$$

where ΔE is the energy difference between the two states, $\hbar$ is the reduced Planck constant, and λ represents the wavelength.

In low Z plasmas it can be difficult to perform line radiation spectroscopy, as fully ionized atoms will have no bound electrons left. Z corresponds to the atomic number and represents the number of protons. Zap-HD forms a hydrogen plasma with Z=1, so impurities are needed to see line radiation. In the past, methane or other gases would be injected along with hydrogen to 'dope' the plasma with impurities. The current nosecone on Zap-HD is graphite, so doping is not needed as carbon impurities are already present from sputtering and other plasma material-interactions with the nosecone [18]. With Z = 6, carbon has enough ionization states to prevent being fully ionized as the temperature in the pinch rises.

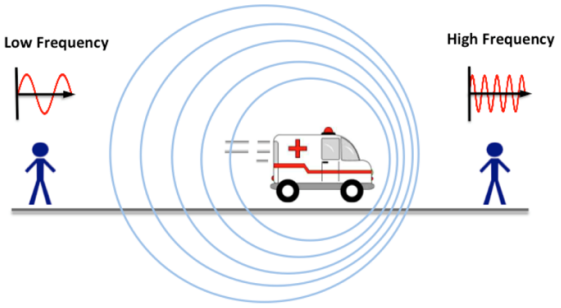

Figure 2.2: An illustration of the frequency shift of an ambulance due to motion relative to an observer. This is an example of the Doppler shift that many people experience in their day to day lives [19].

2.1.1 Measuring Ion Velocity With Doppler Shift

The Doppler shift is an effect that everyone has experienced at some point in their life whether they knew the name for it or not. An example most people have experienced is the increasing and decreasing pitch of a siren as an ambulance or firetruck speeds past. As the source of the waves moves closer to an observer the frequency increases, as the source is moving in the same direction as wave propagation. Once the source has passed an observer and moves further away, frequency decreases, as the source is now moving opposite of the wave propagation with respect to the observer.

Any type of wave propagation will behave with this effect. Since light behaves with wavelike properties, this effect can be taken advantage of to determine the velocity of the plasma in the Z pinch. Wavelength and frequency are related by $c = \lambda\nu$, where λ represents wavelength, ν represents frequency, and c is the speed of light. The Doppler shift in frequency corresponds likewise to a shift in wavelength as the distance between wave fronts increases or decreases. The wavelength is blueshifted for a source moving toward the observer and redshifted for a source moving away. For an optically emitting plasma, the wavelength shift from a known impurity line

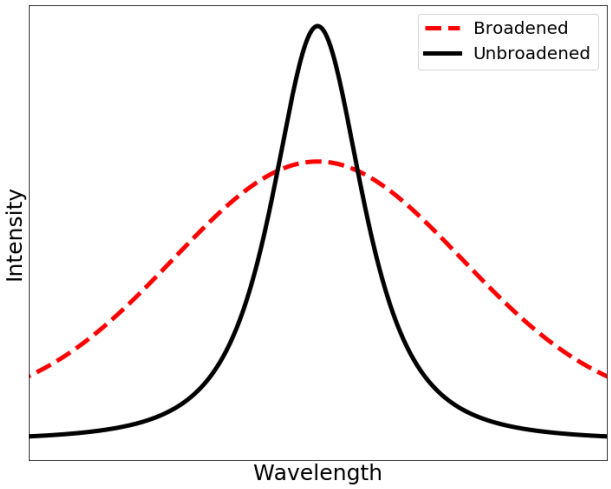

Figure 2.3: Doppler broadening effect is shown in wavelength space for an arbitrary Gaussian distribution.

radiation can give information about the bulk velocity of the plasma.

$$v = c\left(\frac{\Delta\lambda}{\lambda_0}\right)\frac{1}{cos\theta} \tag{2.2}$$

The velocity of the impurity ions in the plasma can be found using Eq. (2.2). Where $\Delta\lambda$ is the shift in wavelength, λ_0 is the stationary wavelength of the ion, and $cos\theta$ accounts for viewing angles non parallel to the flow of plasma. Here θ is the angle the viewing chord makes with the axial plasma flow.

2.1.2 Measuring Ion Temperature With Doppler Broadening

The distribution function of a plasma species always relaxes to a Maxwellian/Gaussian as a consequence of the Boltzmann-H Theorem [20]. Temperature is a measure of the average kinetic energy of particles in a system. A higher temperature means more higher energy particles and a lower temperature means less high energy particles. In terms of a distribution function in velocity space, a higher average kinetic energy means a wider distribution function. For a distribution in wavelength space the same broadening is seen due to the cumulative effect of each particle's wavelength

being shifted slightly due to the Doppler effect. For a species s in local thermodynamic equilibrium (LTE), the distribution function in velocity space takes on the following form in one dimension:

$$f_s(v) = n_s \left(\frac{m_s}{2\pi k_B T_s} \right)^{\frac{1}{2}} exp \left[-\frac{m_s (v - v_0)^2}{2 k_B T_s} \right] \tag{2.3}$$

Using the Doppler shift to solve for velocity in terms of wavelength shift and calculating the resulting wavelength space full width at half maximum gives:

$$\Delta f_{FWHM} = \left(\frac{k_B T_s ln2}{mc^2} \right)^{\frac{1}{2}} f_0 \tag{2.4}$$

Expressed in terms of wavelength, as the Gaussian distributions will be in wavelength space:

$$\Delta \lambda_{FWHM} = 2 \left(\frac{2 ln2 k_B T_s}{m_s c^2} \right)^{\frac{1}{2}} \lambda_0 \tag{2.5}$$

Rearranging and converting to units of electron-volts, the temperature of the species s is:

$$T_s(eV) = (\Delta \lambda_{FWHM})^2 \left(\frac{m_s c^2}{4 ln2 e \lambda_0^2} \right) \tag{2.6}$$

where T_s is the temperature of the species, $\Delta \lambda_{FWHM}$ is the full width at half maximum (FWHM) of the Gaussian distribution in wavelength space, m_s is the mass of the species, c is the speed of light, and e is the elementary charge.

2.2 Deconvolution Methods for Chord Integrated Spectroscopy

Plasma columns in a Z pinch are generally assumed to be axisymmetric with radial shells of constant plasma parameters. The raw spectroscopy results are useful, but are a chord integrated result. This means the camera sees contributions from each plasma shell that the chord goes through.

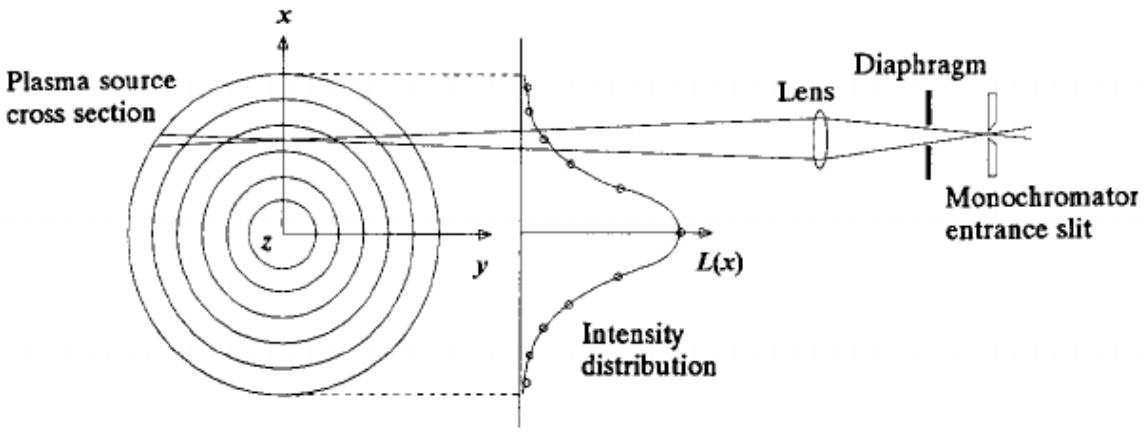

Figure 2.4: A diagram depicting a plasma column as concentric shells showing how the chord integrated aspect of spectrometer measurements depends on the amount of shells the chord passes through [21].

The center chord spectra will have the highest intensity as it is a convolution of light across the entire plasma width. The outermost chords are assumed to go through only one plasma shell, so the intensity will be lower as it contains no convolution and is the Gaussian of a single shell as opposed to multiple shells convolved together. While the chord integrated spectra does give useful information, generally, a radially varying profile of the plasma is wanted. In order to find the radial plasma parameters a deconvolution of the shells is implemented. Deducing the radial distribution of chordal measurements in a cylindrically symmetric plasma where parameters are independent of θ and z in a cylindrical coordinate system (r, θ, z) is possible through the mathematical properties of the Abel transform.

The Abel transform works by starting at the outermost chord, which is assumed to go through only one plasma shell, and then working inward and subtracting the contribution of this outer shell from the next chord inward based on the length of the chord through the outermost shell. The second outermost shell value is now known and the next shell inward can be computed by subtracting the contributions from the two outermost shells. This process continues all the way into the center-most chord, which is assumed to have contributions from all the outer chords [22].

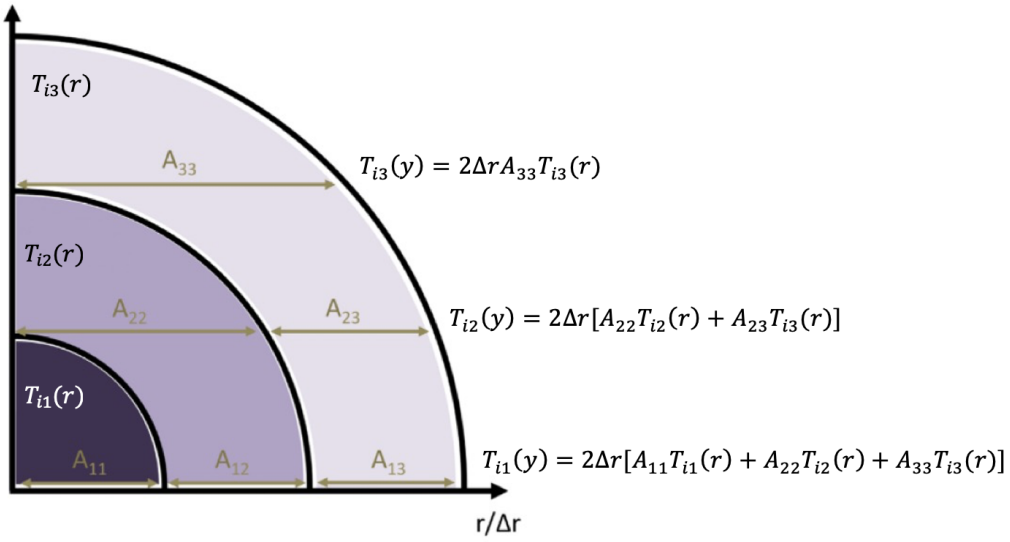

Figure 2.5: Breakdown of the Abel transform for chord integrated ion temperature $T_i(y)$. The plasma is broken down into concentric annular regions of constant temperature $T_i(r)$ where the length of the chord through that region contributes directly to the chord integrated value. Three arbitrary chords are chosen for example, but this process scales for n number of chords

The inversion is performed on both sides of the center chord, which corresponds to the center of the pinch axis. Each side can then be compared and if there are differences in the plasma parameters on one side from the other it means that the center and edge chord were not correct. The geometry is adjusted and the process is repeated until the calculated parameters converge within bounds set by the user. For a radially constant parameter $f(r)$ the chord integrated value $F(y)$ given by the measured spectra

$$F(y) = \int_y^a f(r) \frac{rdr}{(r^2 - y^2)^{\frac{1}{2}}} \tag{2.7}$$

which can be discretized as

$$\vec{F} = \Delta r \boldsymbol{A} \vec{f} \tag{2.8}$$

if $\vec{f}$ is uniform in each annular region, where $\boldsymbol{A}$ is a length matrix composed of the contribution of each plasma shell to the total length of the chord through the plasma and Δr is the distance

between chords [23; 24]. Now that the equation is in matrix form, it is simple to find $\vec{f}$ with an inversion of matrix $\boldsymbol{A}$:

$$\vec{f} = \frac{\vec{F}}{\Delta r}\boldsymbol{A}^{-1} \tag{2.9}$$

For example, the Abel inversion of ion temperature T_i for the geometry shown in Fig 2.4 results in

$$\vec{T_i}(r) = \frac{\vec{T_i(y)}}{2\Delta r}\boldsymbol{A}^{-1} \tag{2.10}$$

with the chord integrated measurements seen by the camera given as $\vec{T_i}(y)$ and the desired radially resolved measurements as $\vec{T_i}(r)$. The factor of 1/2 in Eq. (2.10) accounts for the geometry shown over a quarter of a circle in this example, so the full lengths in the length matrix require a factor of 2. The inverse Abel transform works for any number of chords and works for any chord angle. If the chord angle is changed the geometry shifts from circular regions of constant parameters to elliptical regions. The geometry shift simply requires dividing matrix $\boldsymbol{A}$ by a constant $sin\theta$, where θ is the angle made by the chords and the z-axis of the plasma. $\theta = 45^o$ for the oblique telescope.

Finding the radial temperature profile requires dealing with the inherent broadening imparted by the instrument used to capture the spectra. Each device has a unique instrument function associated with it that varies by chord. In order to find the true temperature of the plasma, the instrument function must be found for each chord. This was done using a still frame of a cadmium (Cd) calibration lamp with the spectrometer looking at the 228.8 nm wavelength line. Because the instrument function is not a Gaussian or Lorentzian function, we cannot simply subtract the instrument function's FWHM from the Gaussian FWHM of the ion emission at each temperature chord. A process for spatial deconvolution to obtain temperature and velocity profiles from chord integrated spectra created Golingo and Shumlak can be used instead to solve this problem [25]. The process is similar to the Abel inversion and also consists of creating a length matrix of the shell contribution at each chord. Instead of performing inverse matrix multiplication on a plasma parameter, however, this deconvolution process involves fitting an instrument broadened Gaussian

to the data from each chord and then subtracting the fit of outer shells from that of inner shells. The fitted spectra of the outer shell are weighted by the length of the chord passing through that shell divided by the total length of the chord passing through all shells and then subtracted from the inner shells fit. The geometry of the shells is the same as the Abel inversion geometry shown in Fig 2.5.

CHAPTER 3

EXPERIMENTAL APPARATUS

3.1 High Speed Camera Use for Fast Framing Spectroscopy

In order to capture multiple images from the same plasma pulse a high speed camera replaced the Pi-Max 4 P43 Intensified Charge-Coupled Device (ICCD) typically used for spectroscopy on ZaP-HD. The Phantom T2410 high-speed camera used in this thesis comes equipped with a 1280 x 800 pixel Complementary Metal Oxide Semiconductor (CMOS) Back Side Illuminated (BSI) sensor equating to 18.5 μm pixel size. Like CCDs, CMOS sensors are semiconductors that take advantage of the photoelectric effect to convert light into electrical signals. They differ mainly in how they convert the initial charge signal into a digital signal. CMOSs have individual amplifiers coupled to each photodiode unlike CCDs. This lowers power consumption and improves speed of signal processing at the cost of additional noise [26]. The back illumination aspect of the sensor is a way to increase CMOS performance in low-light conditions by putting the active matrix and its wiring behind the sensor instead of in front.

The acquisition of data for the T2410 follows that of most modern cameras. The array of sensors/pixels set the resolution for the camera and during each frame acquisition a number of photons are converted to a number of electrons. The ratio for the amount of electrons generated per photon is the quantum efficiency of the camera. A quantum efficiency of 1 is ideal; however, this value will always be below one in practice. As visible light hits the sensor, a certain number

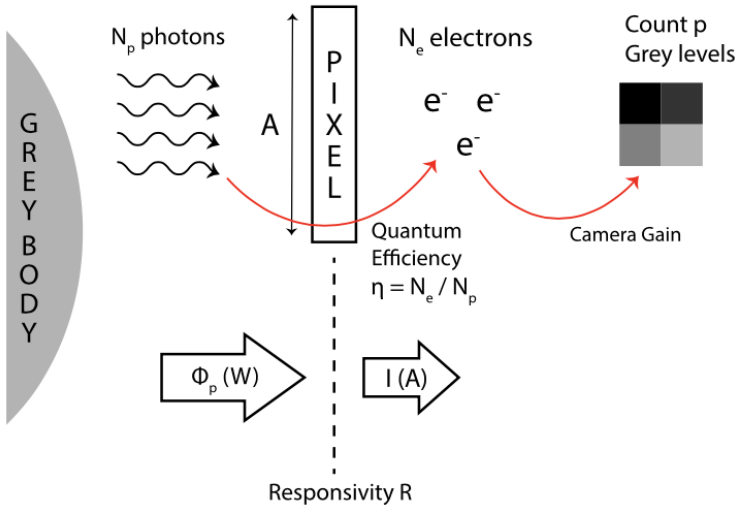

Figure 3.1: Schematic showcasing the photoelectric effect and how incident light is converted into a grey scale pixel value [28].

of electrons are produced proportional to the photon flux through the individual pixel. At the end of each exposure, the electrons are converted to a voltage, which in turn produces a digital signal. The data in this thesis is saved as tiff files containing 2-D arrays corresponding to the pixel array of the sensor. Each index in the array contains a number from 0-255 for each pixel corresponding to the intensity of light in the image in grey scale, where 0 is black and 255 is white. Though the wavelength used for this research is in the ultraviolet (UV) range, an image intensifier added to the setup allows the T2410 to capture light from the plasma in the visible range. Fig 3.2 outlines the color and monochrome quantum efficiencies per wavelength. A value of around 80% is seen for the visible light range, so it is assumed that about .8 electrons are produced for each incident photon. The efficiency is not perfect, but a quantum efficiency anywhere close to 1 is adequate for experimental research [27].

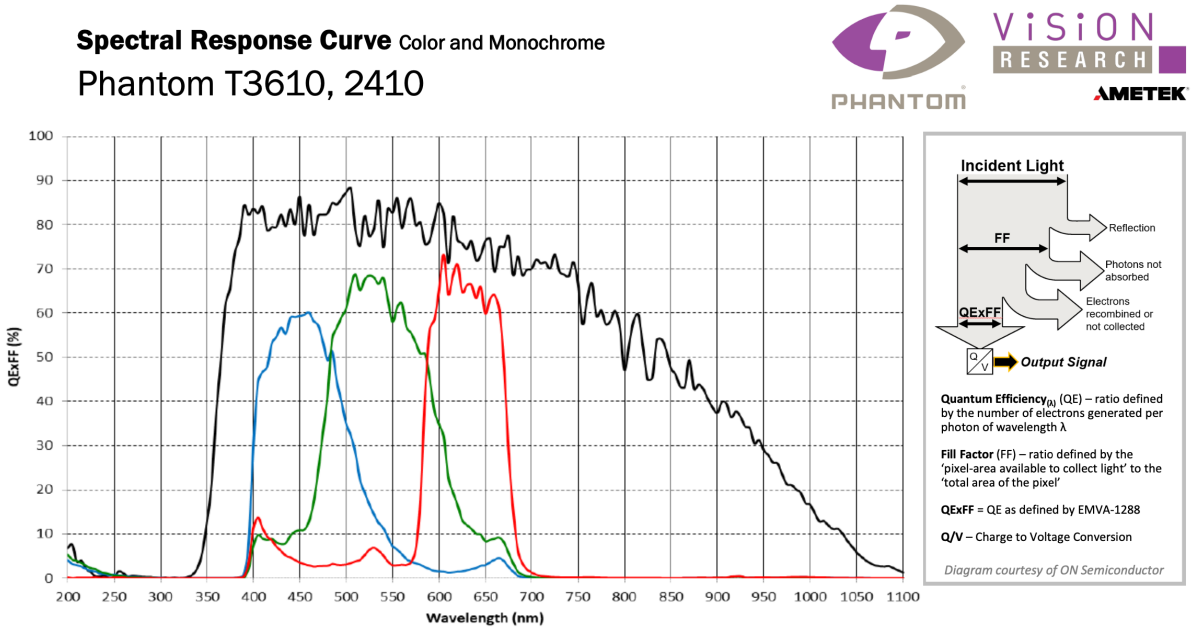

Figure 3.2: Quantum Efficiency for color and monochrome. Can see about .8 electrons for every photon in the visible light wavelength range.

3.2 Investigating Non-visible Light With an Image Intensifier

Initially work was done looking at visible light emission from the plasma. A C III line at 462.47 nm was investigated, however there were too many spectral lines within a close range of that wavelength. The C III line was unable to be differentiated even at extremely high spectral resolution due to being part of a C III triplet and also being close to copper and tungsten line radiation. Another line had to be picked outside of the visible range, where plasma impurity emission is less common and it is easier to find a lone spectral line. The C III line at 229.687 fit this criteria. The T2410 has an extremely low quantum efficiency in the UV range as seen in Fig 3.2, so an image intensifier was necessary to investigate the spectra.

Image intensifiers are common in many disciplines. ICCDs, night vision goggles, and medical X-ray scans are all examples where image intensifiers are used to convert light from the non-visible

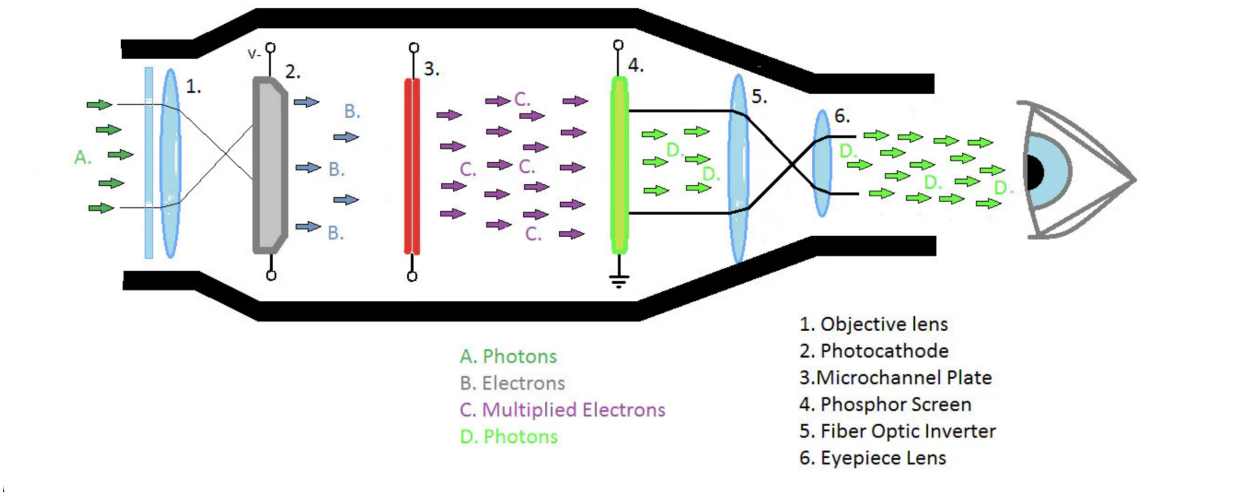

Figure 3.3: 1. Photons enter the image intensifier and are focused onto a photocathode. 2. The photons are converted into electrons as they hit the photocathode. 3. Electrons move through the photomultiplier which increases the number of electrons through secondary electron emission. 4. The increased number of electrons then hit a phosphor screen which releases photons of visible light 5/6. The visible image is then focused onto a sensor of some sort represented by an eye in the image [29]

to visible range, or simply enhance low-light conditions. They function by increasing the number of electrons emitted by an incoming source of photons and accelerating them into a phosphor that gives off visible wavelength photons. Fig 3.3 details the basic steps of an intensifier device.

A Specialised Imaging SIL3 image intensifier was used for the work done in this thesis. The SIL3 uses a P46 phosphor screen to output visible light at 536 nm wavelength. A composition of cerium and yttrium aluminum garnet (YAG) make up the P46 phosphor. Though P46 is less efficient than other commonly used phosphor screens, it has the advantage of a very small decay time of $\sim$300 ns. This makes it useful for high speed applications in order to avoid ghost images on frames after an initial phosphor activation.

3.3 Experimental Setup for Spectroscopic Measurements

In addition to the intensifier and camera, a 0.5 m Czerny-Turner Acton SpectraPro spectrometer to separate incoming polychromatic light into distinct wavelengths so the camera can see the wavelength of interest, 229.687 nm in this case. A diffraction grating accomplishes this task inside the spectrometer. Different wavelengths are diffracted different amounts, allowing incoming light to be broken up into a spectrum of individual wavelengths. When light encounters closely spaced slits or grooves it spreads as if originating from point sources at each slit/groove. This leads to constructive and destructive wave interference. For each wavelength there is a specific direction from the grating that leads to constructive interference. Setting a wavelength of interest for the spectrometer turns the grating such that the sum of constructive interference is at its peak for that wavelength as given by the following relation:

$$m\lambda = d(sin\theta_i - sin\theta_m) \tag{3.1}$$

where m is the integer propagation mode of interest, λ is the wavelength, d is the center to center distance between grooves, θ_i is the incident angle of the wave and θ_m is the difference between the grating normal vector and the diffraction angle of maximum constructive interference [30]. Three different grating options are available on the spectrometer: 3600 g/mm, 2400 g/mm, and 150 g/mm. The unit g/mm represents the amount of grooves per millimeter on the grating itself and the higher this number, the higher the resolution of the spectra. As the resolution increases, the field of view decreases, meaning a smaller range of wavelengths is seen. In the case of this thesis, only one spectral line is of interest. For this application, resolution is more necessary than a higher field of view, so 3600 g/mm is used.

Two telecentric telescopes mounted on the rectangular window on top of the machine's assembly region are connected to a fiber bundle that leads light into the spectrometer. One is mounted

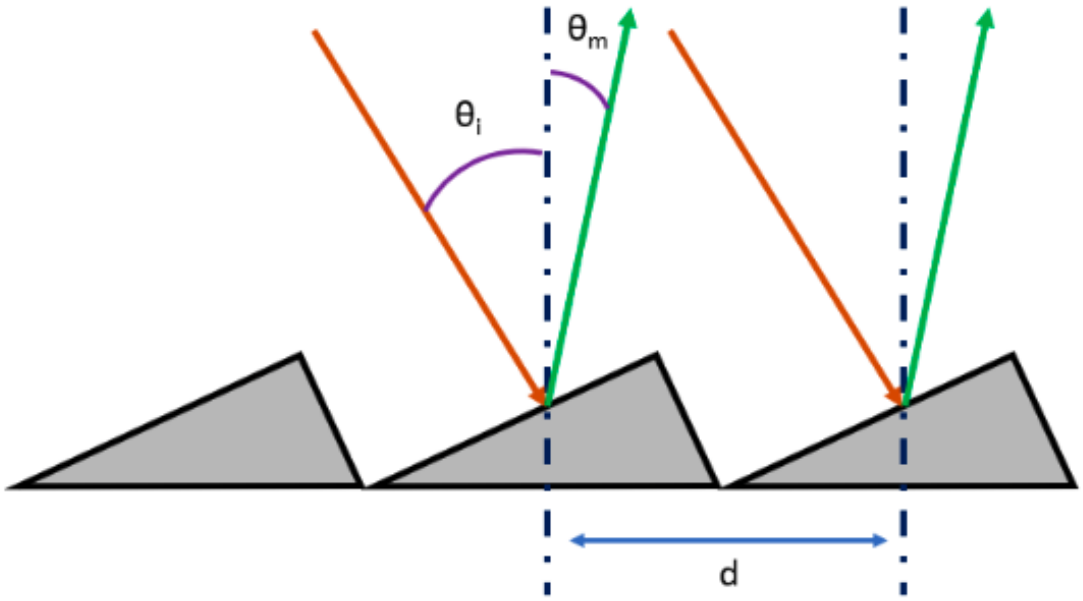

Figure 3.4: Geometry of a diffraction grating with grooves. Grating is turned so that wavelength of interest constructively interferes on spectrometer detector [16]

perpendicular to the plasma flow and one is at an angle of 45 degrees to the plasma flow. The telescopes are telecentric to avoid parallax, ensuring that the size of the plasma viewed does not change regardless of distance from the telescope [31]. The fiber bundle used is a split bundle, with 20 total parallel chords on the end of the ferrule going into the spectrometer, which then splits into two bundles of 10 parallel chords each connected to one of the telescopes. The split bundle has an inter-fiber spacing of 2 mm and images 20 mm total across the assembly region. The angled/oblique telescope measures the Doppler shift of impurity lines and the perpendicular/radial telescope measures Doppler broadening. This results in simultaneous collection of velocity and temperature data at the same axial location.

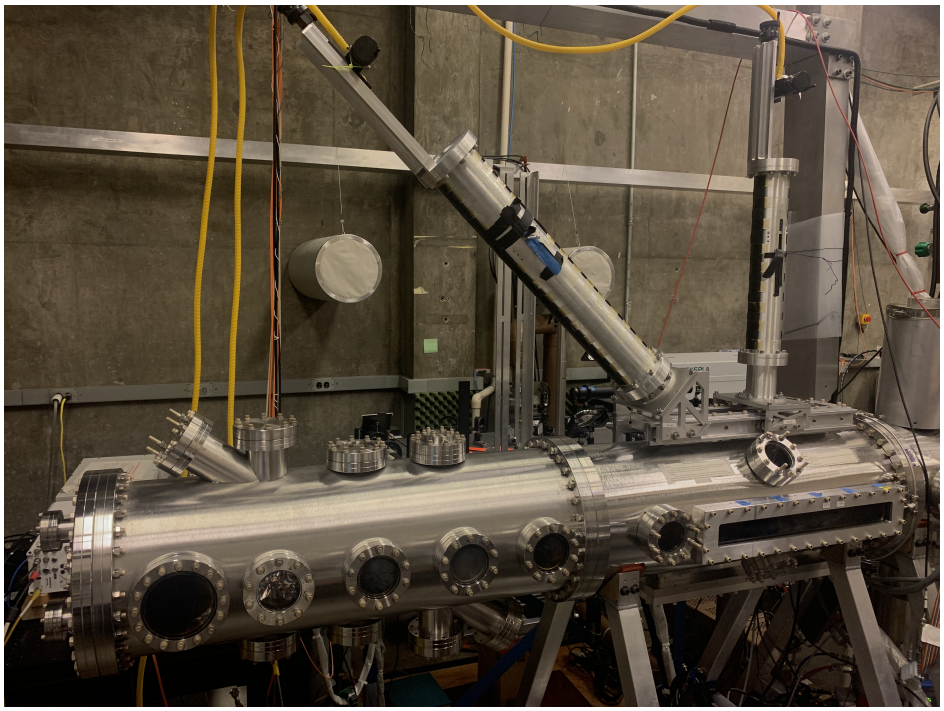

Figure 3.5: Image of ZaP-HD with both the oblique and radial telescope setup to the z = 20 cm axial location.

3.3.1 Calibration of Camera to Wavelength Space

Since the Phantom camera is not a native spectroscopy tool with calibration inherent to its software, a manual calibration is needed to convert pixel space to wavelength space. A cadmium pen-lamp with strong spectral lines of Cd II at 226.501 nm and Cd I at 228.802 nm is useful for its relative closeness to the C III line of interest at 229.687 nm. With two known wavelengths hitting the Phantom sensor it is relatively easy to create a linear mapping of pixels to their corresponding wavelengths by

$$\lambda_{actual} = m\lambda_{observed} + b \tag{3.2}$$

where m, the slope of the linear mapping represents resolution in nm/pixel. Using the 3600 g/mm grating a resolution of .00528 to .00533 nm/pixel is achieved depending on the chord. This gives spatial resolution over twice that of previous time resolved spectroscopy on ZaP-HD.

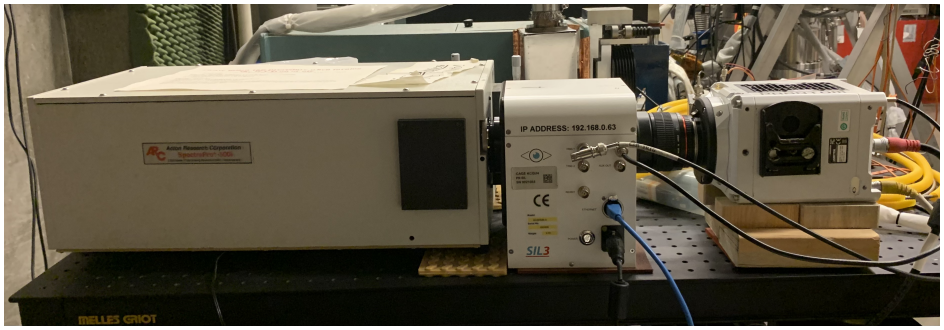

Figure 3.6: Image of spectrometer, intensifier, and Phantom setup.

3.3.2 Instrument Settings for a Plasma Pulse

The impurity ion of interest is the 229.687 nm C III line as stated earlier due to its solitude with no other impurities emitting from the plasma around that wavelength and its abundance in the plasma from erosion of the graphite nose cone. The center wavelength of the spectrometer is set to this and the entrance slit width of the spectrometer is set to 20 μm. The Phantom is set to a resolution of 1280 x 64 pixels to maintain the highest frame rate possible while also having enough spatial resolution to see broadening and shift effects. The SIL3 intensifier is set to 1.22 μs exposure time with 1 μs of separation between phosphor rises. The intensifier can take 64 exposures in burst mode, limiting the number of frames to 64 per pulse. In order to sync the Phantom and the SIL3 so that each phosphor rise corresponds to the shutter of the camera opening, specific settings had to be used. The most repeatable conditions are found by setting the Phantom into external sync mode with a 2.22 μs delay and connecting a BNC from the SIL3's AUX OUT port to the Phantom's FSYNC port. This ensures that the shutter opens with each phosphor rise signal from the intensifier, meaning that each frame sees only one individual phosphor rise and decay and does not see any ghost images from previous frames. An oscilloscope with two channels connected to both the intensifier and the camera is used to confirm the signals from both devices synced sufficiently.

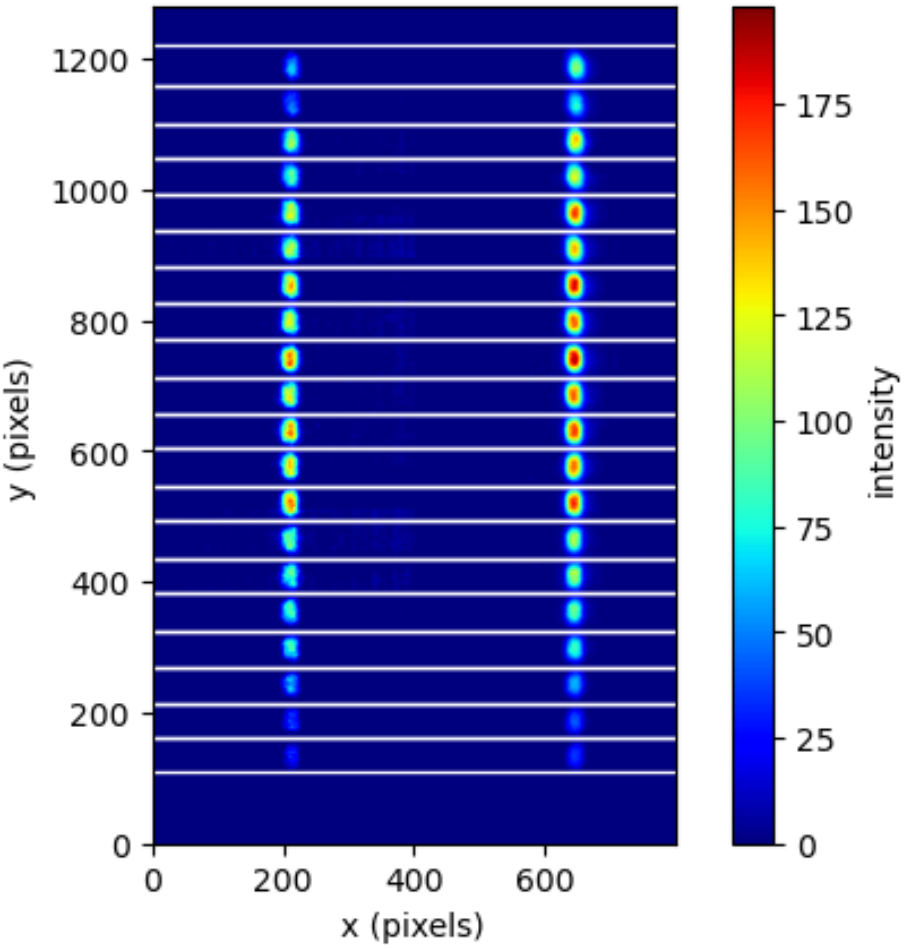

Figure 3.7: Raw Phantom image of Cd calibration lamp. The Cd II 226.501 nm line is on the left and the Cd I 228.802 nm line is on the right. The white solid lines represent the bin edges for velocity and temperature chords. The top chord is a velocity chord followed by the corresponding impact parameter's temperature chord.

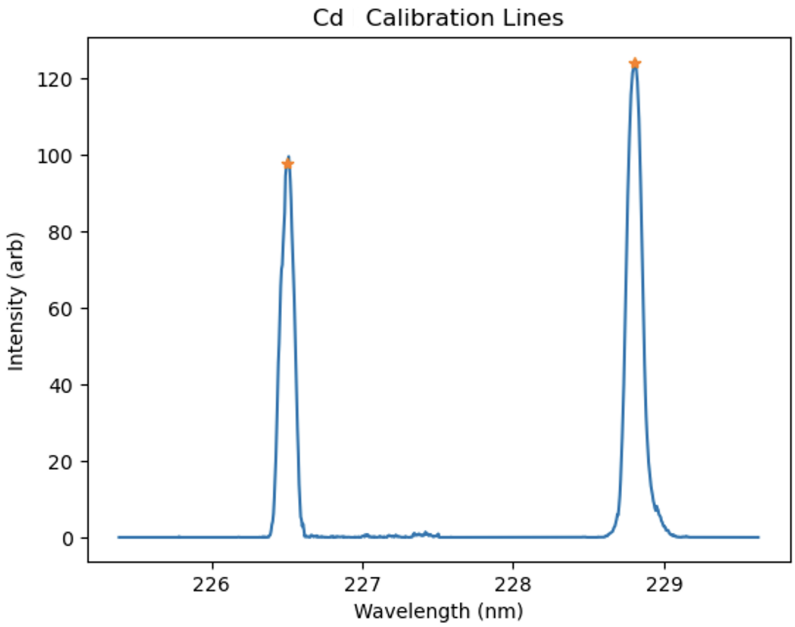

Figure 3.8: Example of the curve fit and corresponding centroid locations labeled by the yellow star for a single chord from the raw phantom calibration image after the linear mapping from pixel to wavelength space

CHAPTER 4

EXPERIMENTAL RESULTS

C III impurity ion radiation at 229.687 nm is used to measure ion parameters for hydrogen plasmas in the ZaP-HD device. Spectrometer entrance slit is $20\mu m$ for all pulses. Both the oblique and radial telescope are located 20 centimeters downstream from the nosecone, at z = 20, where z = 0 corresponds to the axial location of the nosecone.

Wavelength (nm)	State	Electron Configuration
229.687	De-excited	$1s^2 2s 2p$
229.687	Excited	$1s^2 2p^2$

Table 4.1: De-excited and excited states are shown for the electron transition that results in a photon with a wavelength of 229.687 nm from a carbon ion. Data is from the NIST Atomic Spectra Database.

The maximum resolution for the Phantom is 1280 $\times$ 800 pixels with a minimum exposure time of 1 μs. The frame rate can be lowered to 24,270 fps. These settings are used to capture the calibration frame and instrument function frame using the Cd lamp. For recording the plasma pulse, the frame rate needed to be much higher in order to see any time variation between frames and capture the evolution of the pulse. A resolution of 1280 x 64 was used during the pulses to ensure the frame rate could approach 450,000 fps, leading to a frame every 2.2 μs as stated in Section 3.3.2. The Phantom saves files as a '.tif' for each frame of a recorded pulse. This

leads to 50 files per pulse, which are then processed in Python. Each chord is binned, numerically fitted with a Gaussian, and analyzed using the methods in Chapter 2 to find ion velocities and temperatures for each chord in each frame. Fig 4.1 shows an example of raw Phantom data for a single frame from a pulse. The lines represent the chords, starting with an oblique velocity chord at the top followed by a radial temperature chord below it. The chords alternate between velocity and temperature. The output from the Phantom is in gray scale, but is converted to false color and put on the 1280 x 800 resolution pixel-space for easier visual contrast.

The original spectroscopy setup included only the Phantom high-speed camera, a lens, and the spectrometer. A visible wavelength C III line at 464.742 nm was the intended target. However due to the presence of multiple impurity lines within a close distance to the line of interest and the C III line being part of a triplet, it was deemed too difficult to extract any relevant data from the captured spectra. This led to examining non-visible emission from the plasma. The 229.687 nm C III line is in solitude when using 3600 g/mm grating on the spectrometer, so no other impurity lines are visible in the range of wavelengths being looked at. In order to use this line, the UV intensifier described in the previous section is added to the setup. Due to physical limitations, the focal plane of spectrometer did not match the focal point of the intensifier. The focus on the intensifier is adjusted for the best possible results, but the spectra are still not fully in focus. However, by capturing the instrument function at the same exposure time used to capture the plasma emission, the subtraction of the instrument function should lead to accurate results, as the artificial focus broadening is equivalent for the instrument function and the plasma emission. Velocity data are not put through a deconvolution process and stay as chord integrated measurements to better compare to past data. The spatial component of the velocity profiles thus depends entirely on the chord geometry and the chords are not adjusted. Temperature data is deconvolved and thus depends on the location of the plasma at z = 20 and is solved in terms of plasma radius. Three different run parameters are used and compared. Table 4.2 displays the three separate cases, which will be referred to as Case I, Case II, and Case III for brevity in the rest of this thesis. The majority of

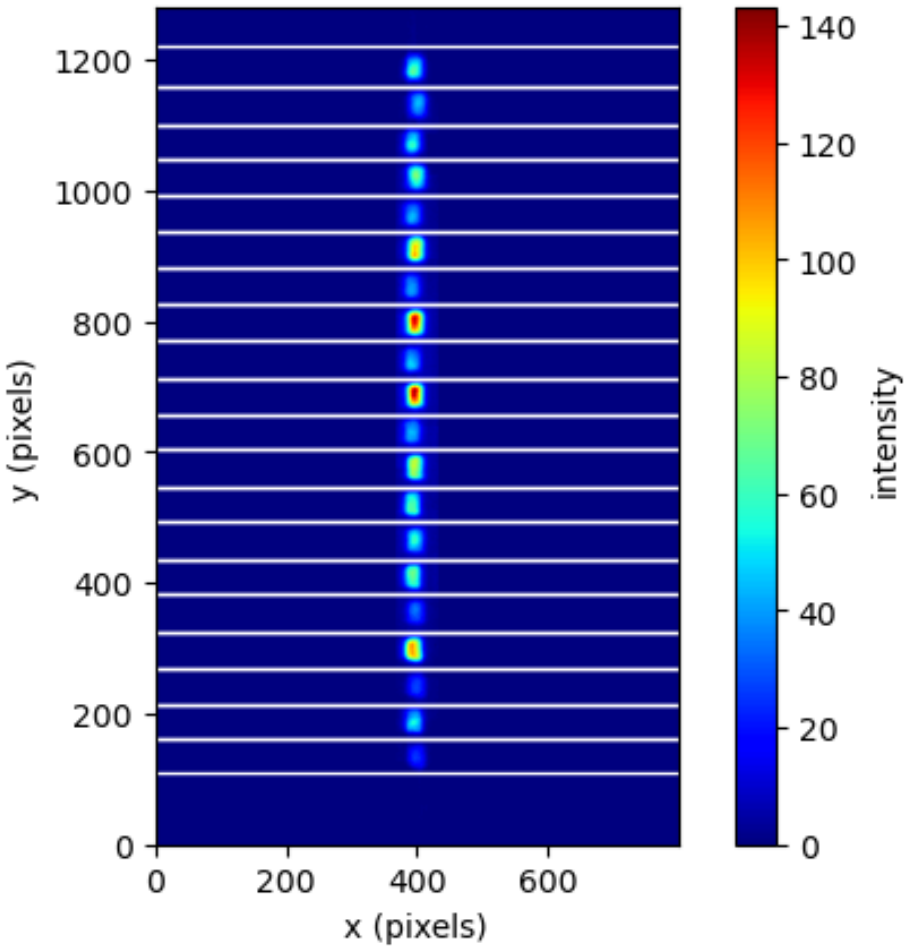

Figure 4.1: A single frame of a Phantom spectroscopy video. The data is from frame 35 of pulse 240506007, which corresponds to $77\mu s$. The raw output from the Phantom is gray scale, but has been converted to color values in Python to make the differences in intensity easier to visualize. The 20 chords are represented by their bin edges, which are shown as solid white lines. The top chord corresponds to velocity, followed by a temperature chord and alternating likewise to the bottom. The velocity blueshift can be seen quite easily in the raw data.

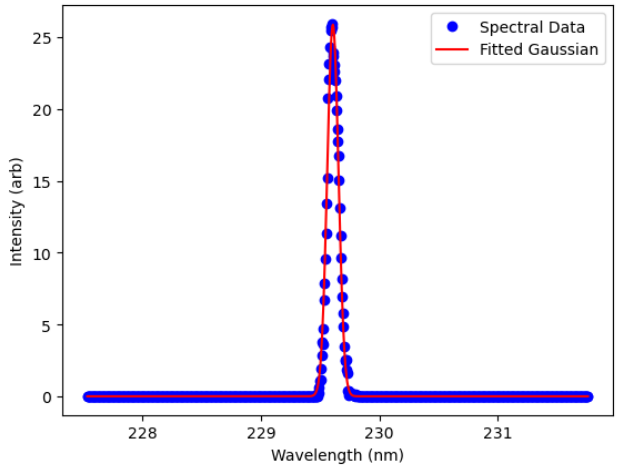

(a) Raw Data and Gaussian Fit for Velocity Chord

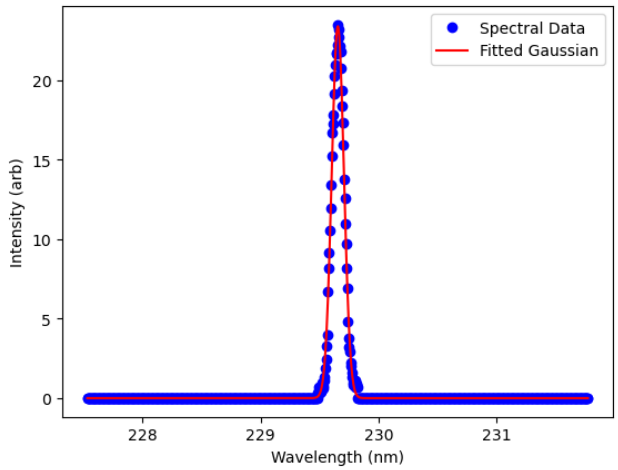

(b) Raw Data and Gaussian Fit for Temperature Chord

Figure 4.2: Raw data from the Phantom is shown from pulse 240506008. Figure (a) shows frame 17, chord 9 from the oblique scope and (b) shows frame 17, chord 7 from the radial scope.

pulses are taken at Case II conditions to maximize the amount of C III present while operating at voltages the machine can handle for heavy repetition. Pulses are taken at lower and higher voltages to see how profiles scale with input power.

Case	Accel. Bank Voltage (kV)	Comp. Bank Voltage (kV)	Peak Pinch Current (kA)
I	7	5	175
II	9	7	240
III	10	10	275

Table 4.2: Values for parameters used for three different run settings for data collection. The only change between cases is the capacitor bank voltages for acceleration and compression discharges.

An initial look at single frames from pulses taken at Case II conditions gives confidence in the results. Fig 4.3 showcases a plasma pinch with higher velocities on the outer chords. Due to the pulse lasting longer than the growth time of the MHD instabilities, shear flow is expected. Fig 4.4 showcases a plasma temperature profile peaked on the plasma axis. This indicates hotter temperatures in the core of the plasma than on the edges, which is also expected. Because of pulse to pulse variability, it is important to take data over multiple pulses in order to confirm results are indicative of a trend. Averaging over multiple pulses helps fill gaps in the plasma profile from poor fits for a single shot. The brightness of the C III varies pulse to pulse giving some more usable data than others. By combining all pulses at a run setting and averaging the data, a more complete profile is resolved. Velocity data labeled relative assumes completely axial flow measured by the oblique scope. Velocity profiles labeled absolute take into account any radial contributions to velocity. Both relative and absolute velocity result in profiles with similar gradients, but differ in magnitude.

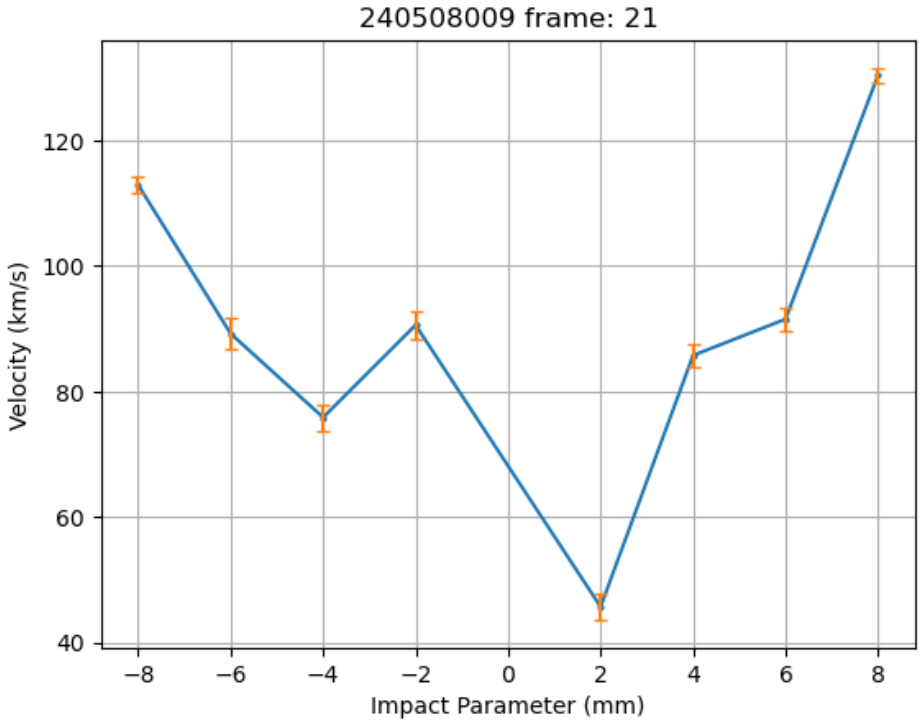

Figure 4.3: A single radial relative ion velocity profile from the plot shown in Fig 4.4 corresponding to pulse 240508009 at 46.2 μs . Measurements indicate velocity peak at the edges of the plasma.

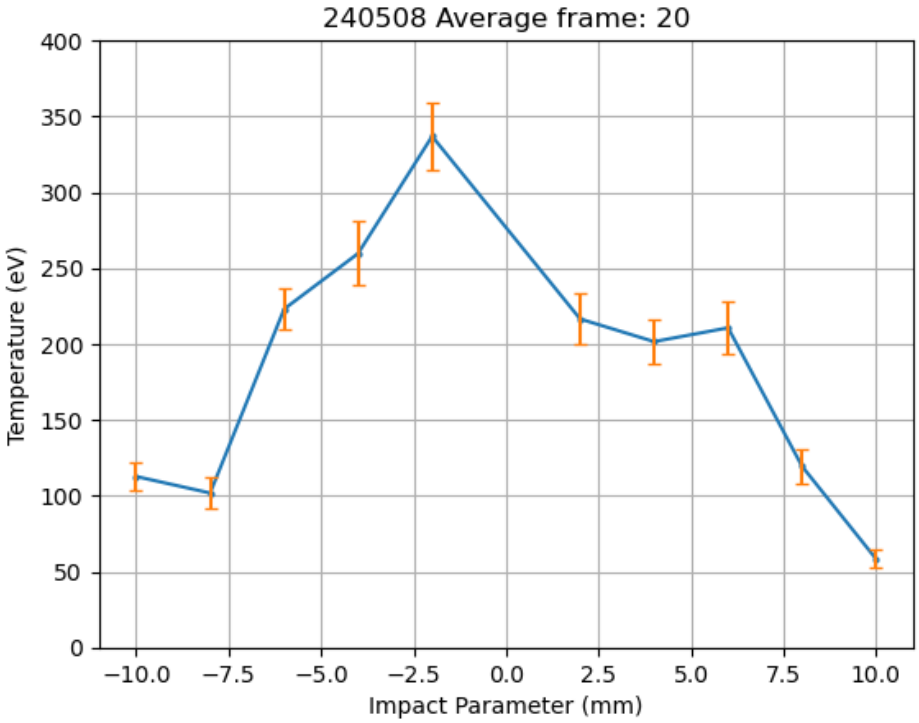

Figure 4.4: A single radial ion temperature profile from the plot shown in Fig 4.9b corresponding to the average of all Case II pulses from 240508007-240508020 at 44 μs . Measurements indicate temperature peak near axis of the plasma.

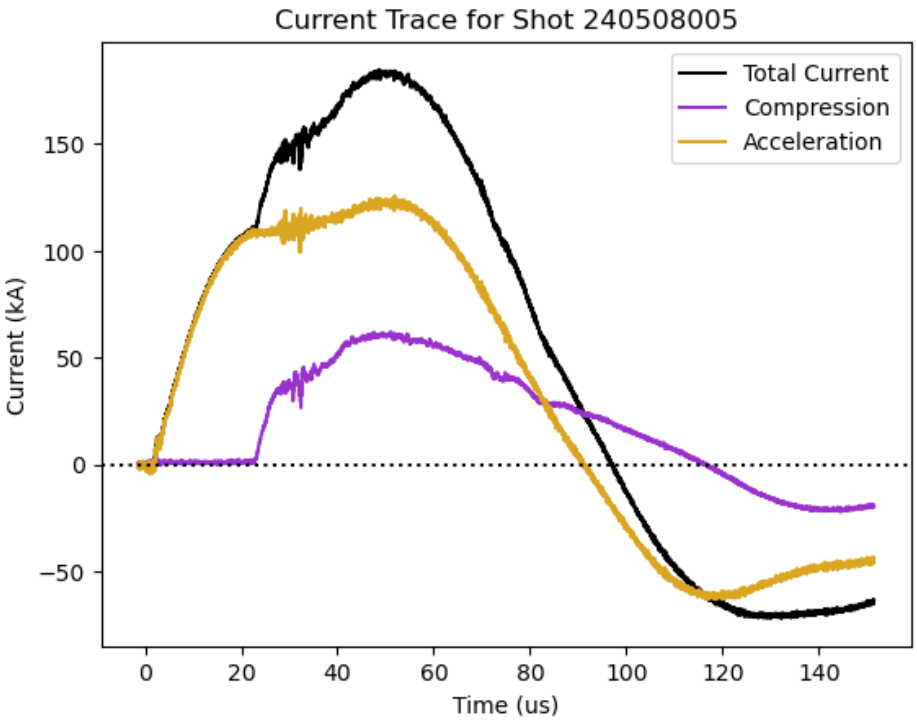

Figure 4.5: Current evolution throughout a single plasma pulse at Case I conditions. Plasma current is the total current with contributions from the acceleration and compression currents. Data is from pulse 240508005.

4.1 Case I Ion Doppler Temperature and Velocity Profiles

If Ohmic heating is assumed as the dominant heating process, the plasma temperature should scale with current. Current and velocity are directly related as well and should scale accordingly. The IDS results for Case I exhibit expected characteristics. Sheared-flow is visible in the profile seen in Fig 4.6. Throughout much of the plasma lifetime the radial gradient is visible. The velocity evolution shows agreement with the current shown in Fig 4.5. The highest velocities around 140 km/s are from $\sim 35\mu s$ to $\sim 60\mu s$ which corresponds to the period of highest plasma current. As the plasma current begins to trend toward zero, the plasma decelerates. Peak temperatures around 150 eV are present in conjunction with the peak compression current and gradually decrease as the current decays. This agreement with expected trends gives confidence in the IDS data.

4.2 Case II Ion Doppler Temperature and Velocity Profiles

Based on the results for Case I and the expected trends with current, Case II profiles should look similar to those from Case I. Fig 4.8a and 4.8b clearly show a completely different velocity and temperature evolution over the pulse duration. Comparing the IDS data with the current trace shown in Fig 4.7 there is no clear trend with current as expected. Instead the velocity profile shows a drop in velocity at $\sim 46\mu s$ when there is not drop in current during that time. The plasma then accelerates, reaching a new velocity peak lower than the magnitude before the drop off. Velocity does seem to drop with the drop in current after this second peak. The temperature profiles show comparably strange behavior. There is seemingly little relation between the plasma current and the IDS data at Case II conditions and instead extreme shifts in the data occur around the same time of $\sim 46\mu s$.

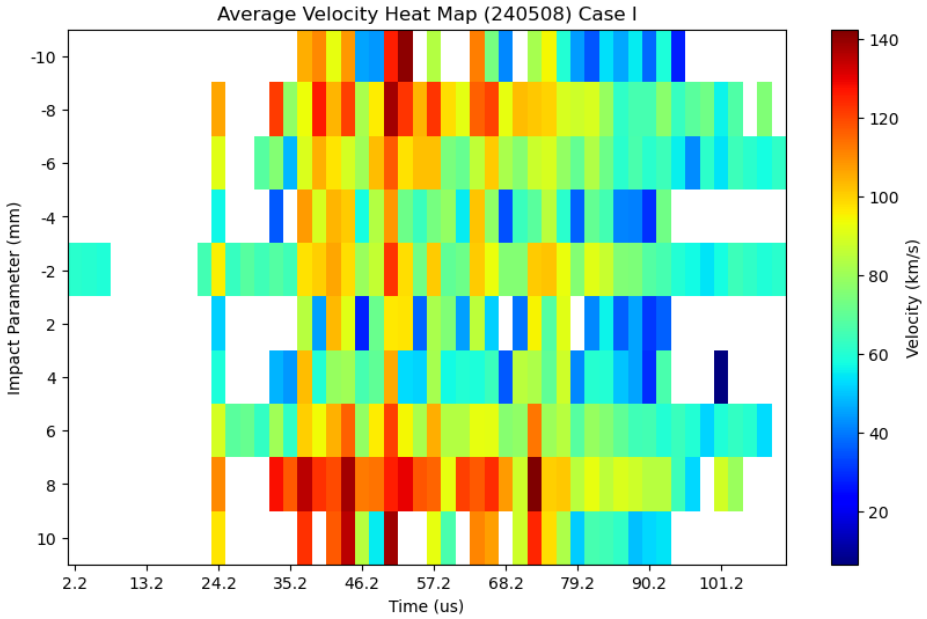

(a) Average absolute ion velocity Case I conditions

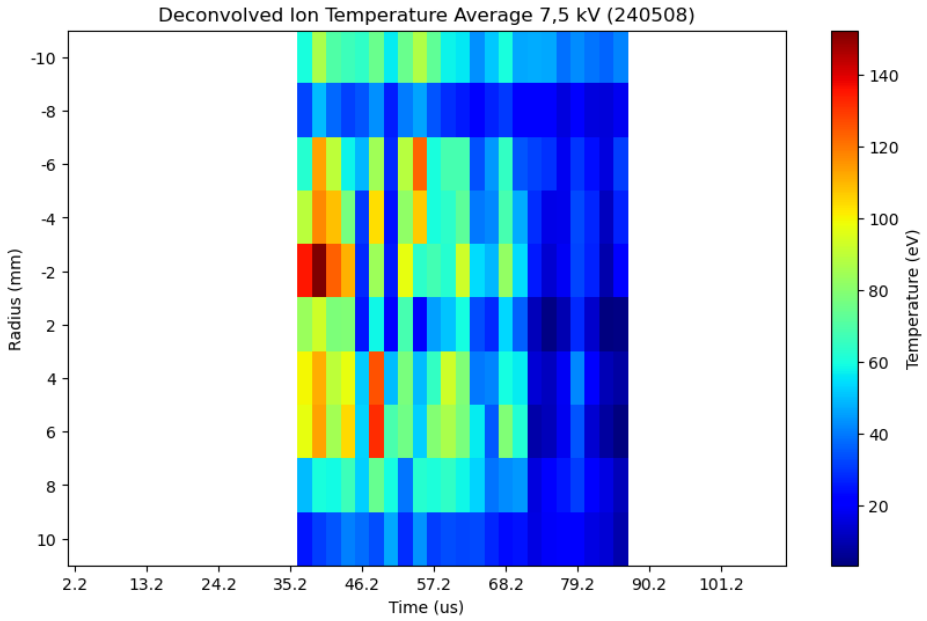

(b) Average deconvolved ion temperature Case I conditions

Figure 4.6: Temperature and velocity profiles from pulses at Case I conditions. Figure (a) is the absolute ion velocity from run day 240508 over pulses 240508004-240508006 and (b) shows the deconvolved ion temperature from the same pulses.

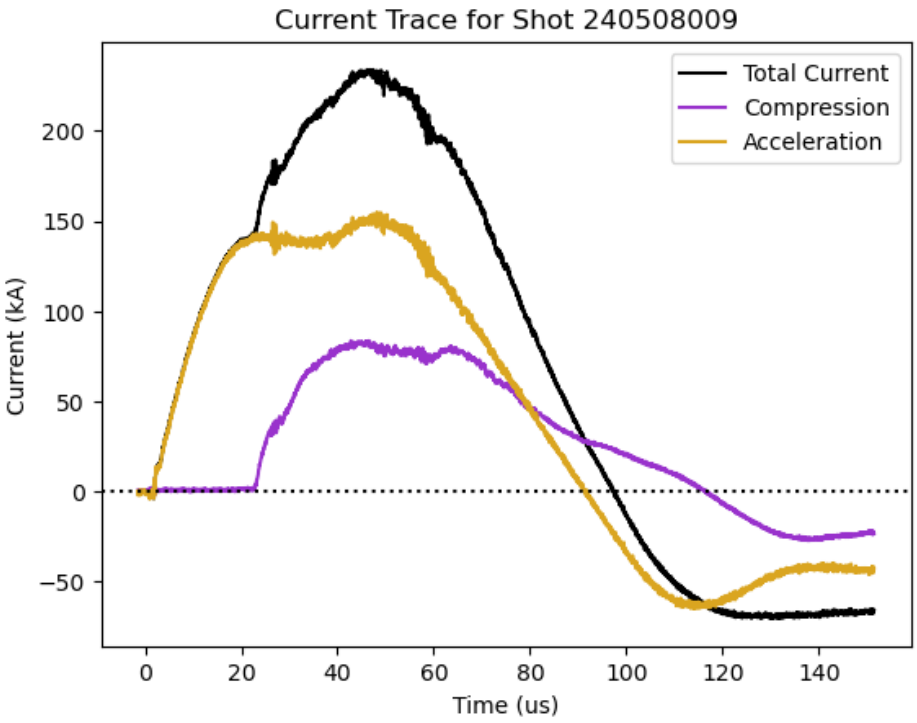

Figure 4.7: A current trace from pulse 240508009 taken at Case II conditions is shown. The total plasma current is the sum of the acceleration and compression current. The total current peaks at 46 μs with a value of 234 kA.

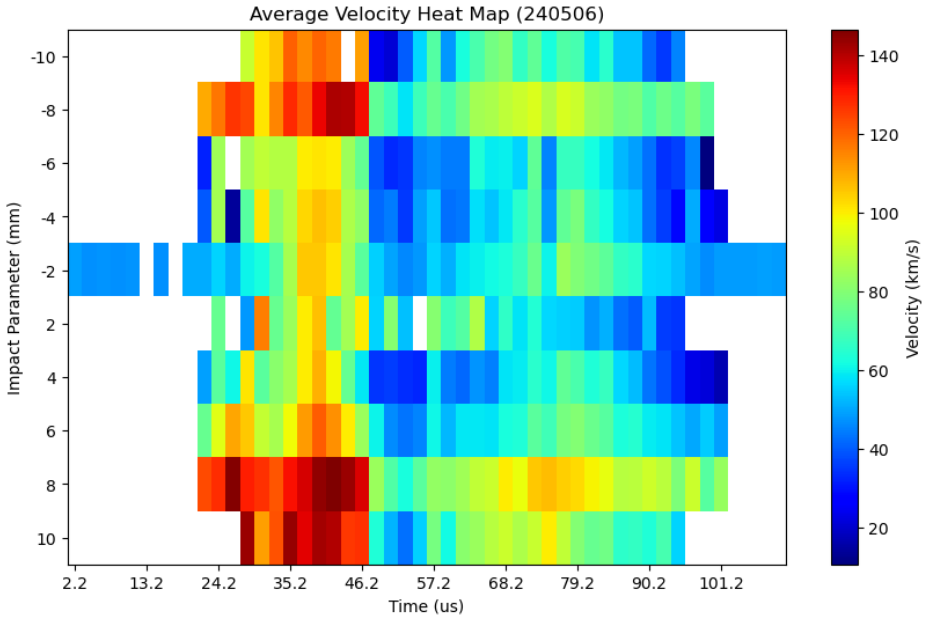

(a) Average absolute ion velocity Case II conditions (240506)

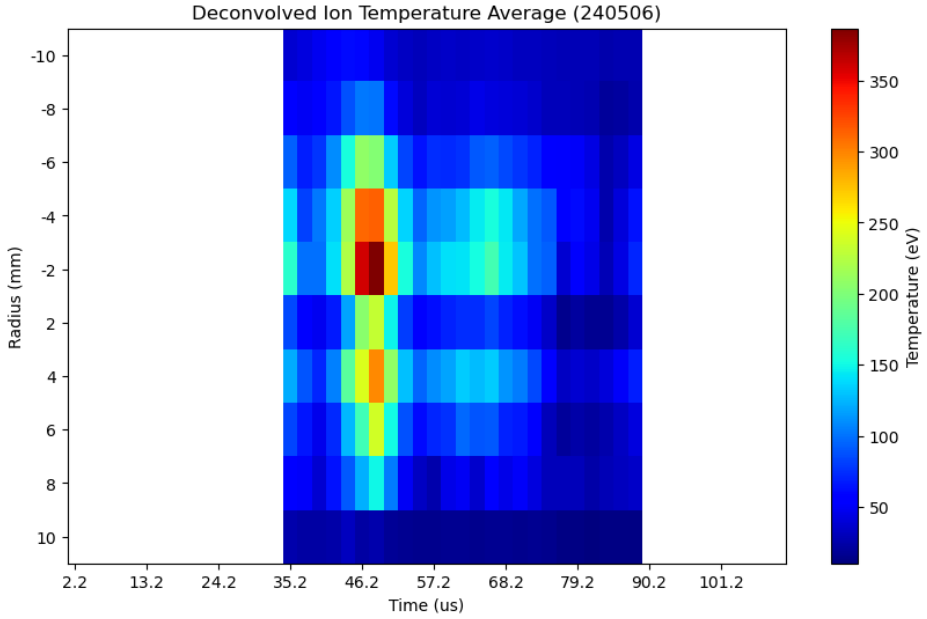

(b) Average deconvolved ion temperature Case II conditions (240506)

Figure 4.8: Temperature and velocity profiles from pulses at Case II conditions. Figure (a) is the absolute ion velocity from run day 240506 over pulses 240506005-240506024 and (b) shows the deconvolved ion temperature from the same pulses.

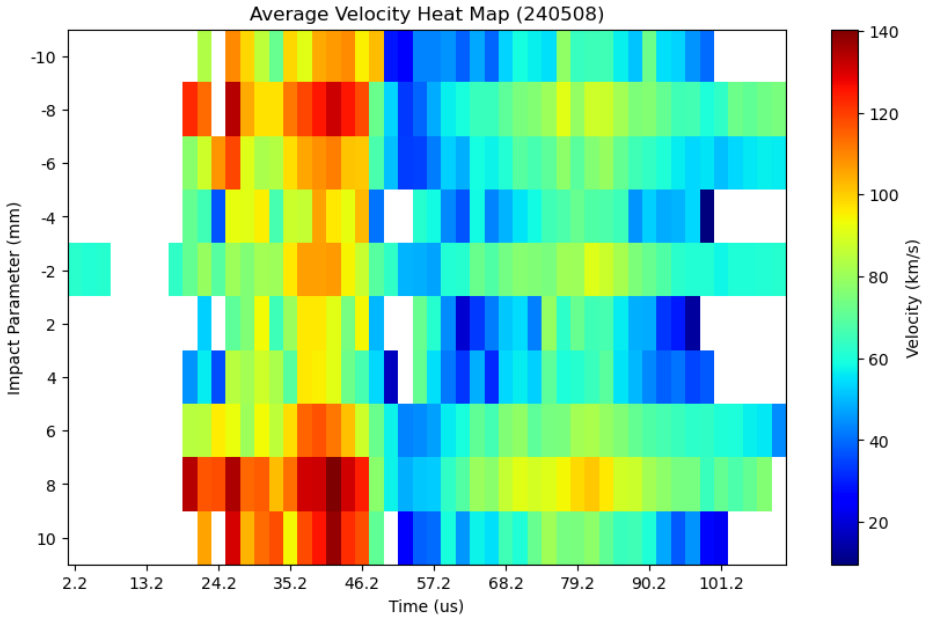

(a) Average absolute ion velocity Case II conditions (240508)

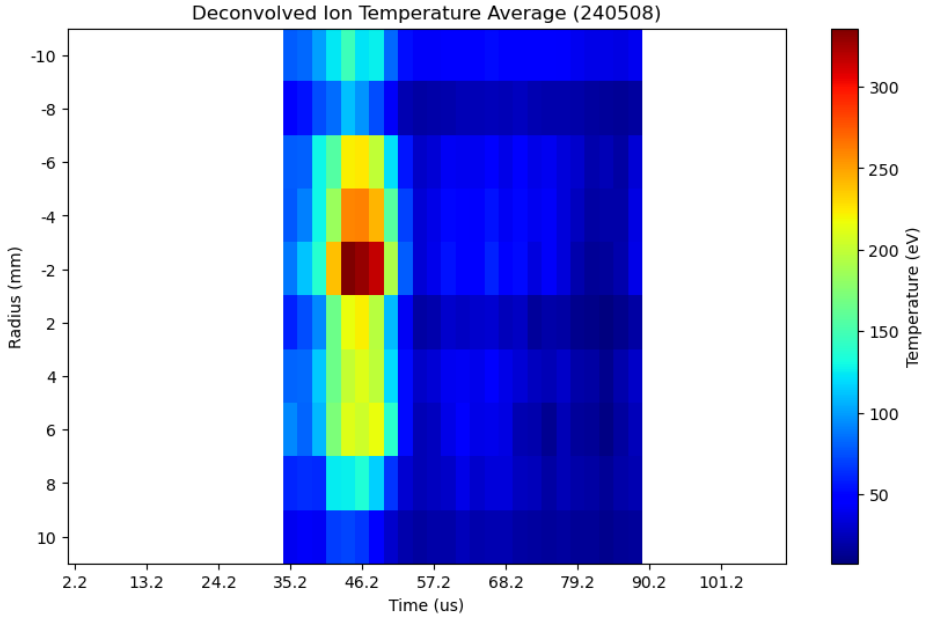

(b) Average deconvolved ion temperature Case II conditions (240508)

Figure 4.9: Temperature and velocity profiles from pulses at Case II conditions. Figure (a) is the absolute ion velocity from run day 240508 over pulses 240508007-240508020 and (b) shows the deconvolved ion temperature from the same pulses.

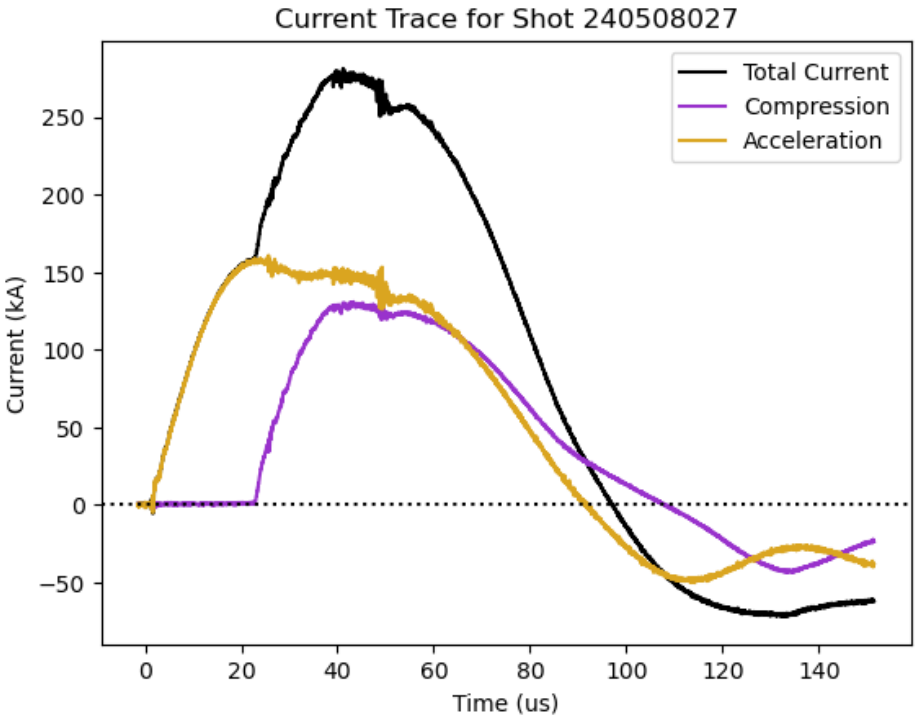

Figure 4.10: A current trace from pulse 240506027 taken at Case III conditions is shown. The total plasma current is the sum of the acceleration and compression current.

4.3 Case III Ion Doppler Temperature and Velocity Profiles

Case III conditions continue the behavior that Case II data exhibits. A drop in velocity and corresponding jump in temperature around the same time is seen in these pulses. The timing of the discontinuity is earlier, at $\sim 40\mu s$ as seen in Fig 4.11. The profiles show similar disagreement with the current trace, however the velocity once again accelerates to a new peak before falling off with current. It should be noted that this second peak velocity is almost 20 km/s higher than the Case II velocity profiles.

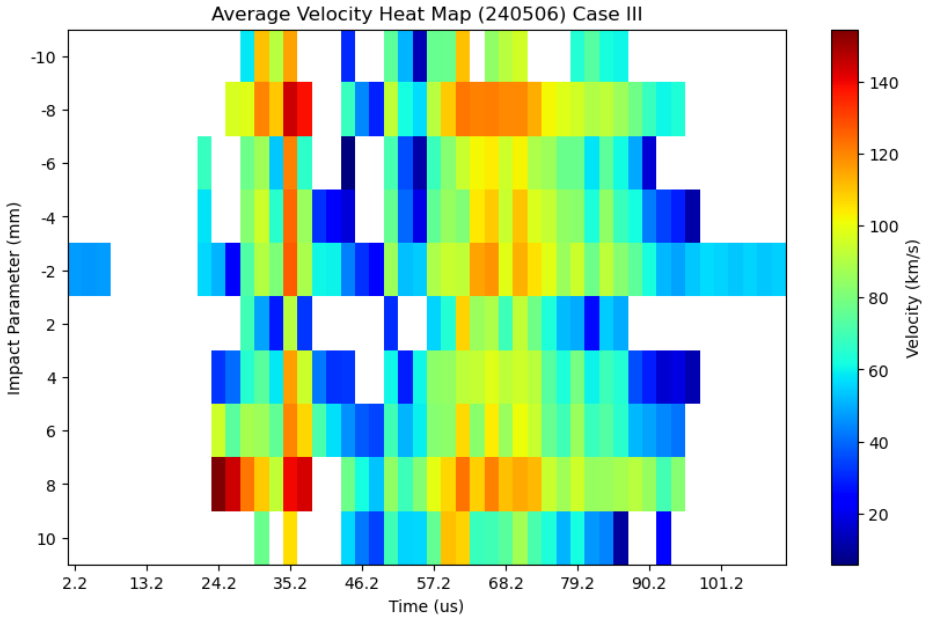

(a) Average absolute ion velocity Case III conditions

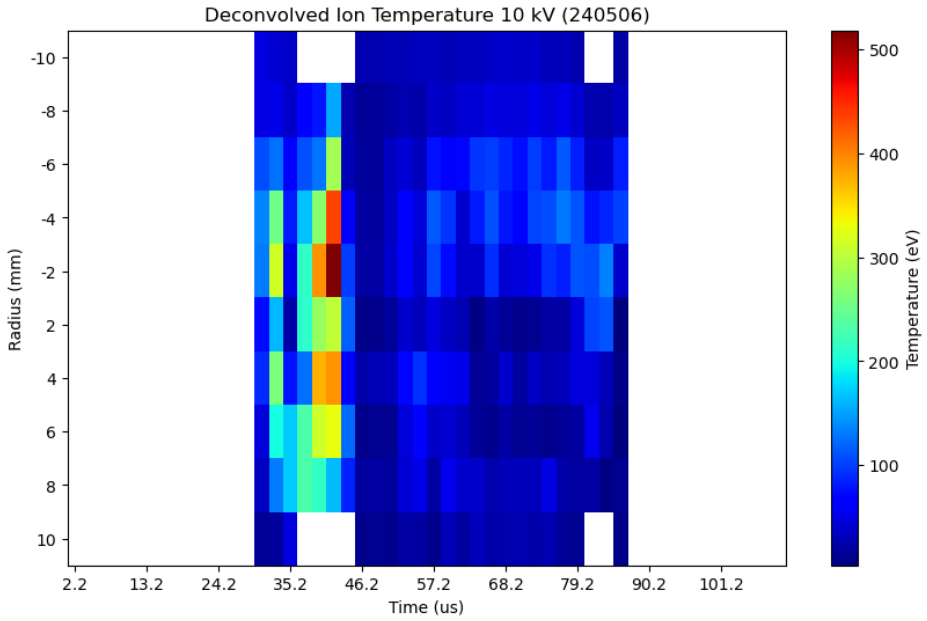

(b) Average deconvolved ion temperature Case III conditions

Figure 4.11: Temperature and velocity profiles from pulses at Case III conditions. Figure (a) is the absolute ion velocity from run day 240506 over pulses 240506026-240506027 and (b) shows the deconvolved ion temperature from the same pulses.

CHAPTER 5

ANALYSIS AND DISCUSSION

The results shown in the previous section give important information on the pinch profile and provide quantitative data relating to sheared-flow for pinch stability. Comparing the results with other diagnostic measurements on ZaP-HD can support the results and give more insight into the plasma pinch behavior. Performance of the Z pinch as a propulsion device can be explored, however without further data, only a general surface level examination is done in this paper.

5.1 Pinch Stability

Magnetic field data is used to determine the stability of the pinch. Magnetic probes in the outer electrode measure time-dependent magnetic field data azimuthally in the assembly region. Magnetic fluctuation levels of the m = 1 azimuthal mode are computed by normalizing the asymmetric component of the field with the symmetric component at the same location, and is given by B_m/B_0. The normalized magnetic fluctuation level is a measure of the radial displacement of the center of the current from the center axis of the machine. Magnetic field probes are aligned at various axial locations to measure magnetic field fluctuations and the average magnetic field magnitude at the outer electrode. Fig 5.2 show large magnetic fluctuations during the pinch formation that subside to low values for a period of 40 μs to 100 μs for Case II pulses on average. Magnetic fluctuations below 0.2 indicate the current centroid is within a centimeter of the machine axis. An extended

period of plasma stability, called the quiescent period, is achieved when the m = 1 mode is below this 0.2 threshold. Fig 5.1 and 5.3 show the magnetic fluctuations for Case I and III pulses. The quiescent periods for these pulses are shorter than Case II pulses.

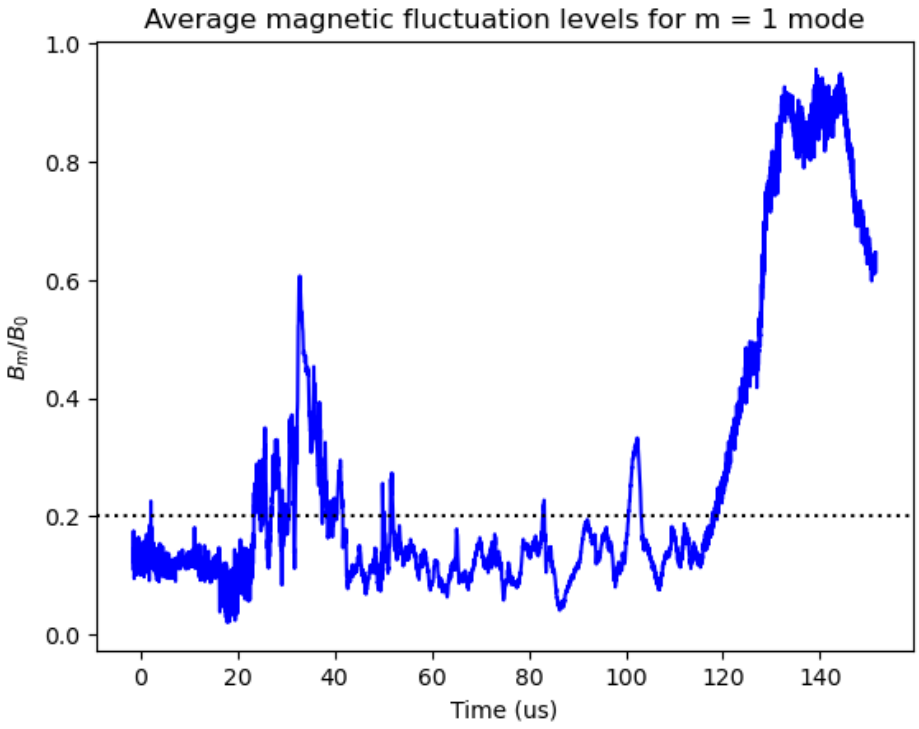

Figure 5.1: Average magnetic fluctuations for the m = 1 azimuthal mode measured at z = 20 cm during a day of plasma pulses. Value at or below 0.2 indicates a centered pinch at the axial location where the IDS data is taken. Data is from pulses 240508004-240508006 at Case I conditions.

The velocity flow shear is clear to see from the contour plots alone in Chapter 4. The required flow shear, $\frac{dv_z}{dr}$, under typical plasma parameters is $5 \times 10^6 s^{-1}$ using $\frac{dv_z}{dr} \geq 0.1 k V_A$ [32]. Fig 5.4 shows a single radial shear profile from a Case II pulse. The measured velocity shear for a frame can be calculated by the difference in adjacent velocity measurements divided by the center to center spacing of the chords. Shear gradients above the threshold are seen throughout quiescent periods for all three cases. The average quiescent periods are magnitudes higher than the instability growth rates, showing that a shear stabilization is in effect.

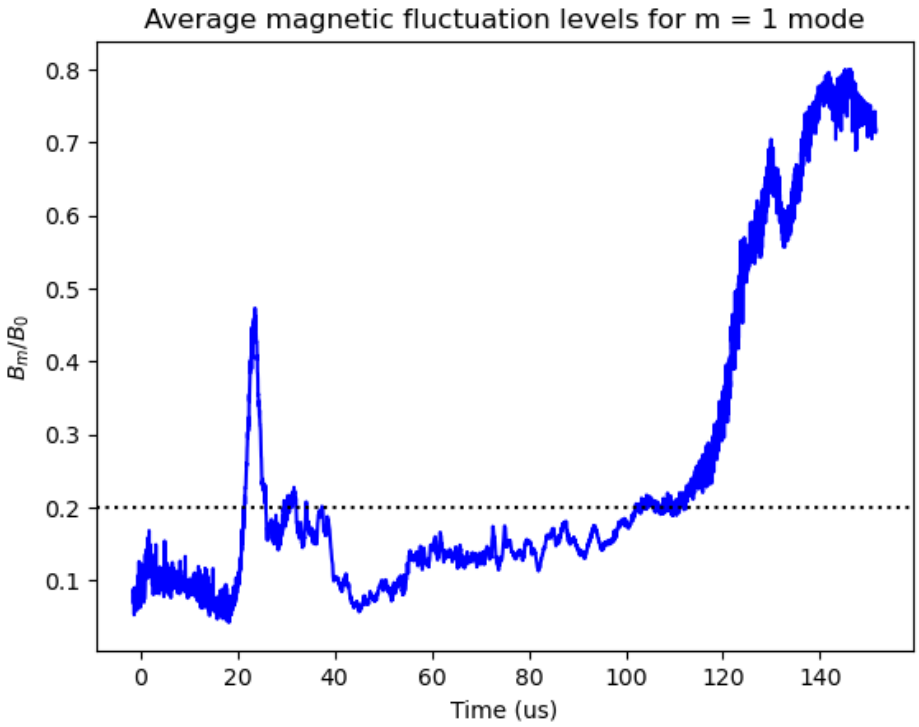

Figure 5.2: Average magnetic fluctuations for the m = 1 azimuthal mode measured at z = 20 cm during a day of plasma pulses. Value at or below 0.2 indicates a centered pinch at the axial location where the IDS data is taken. Data is from pulses 240506005-240506024 at Case II conditions.

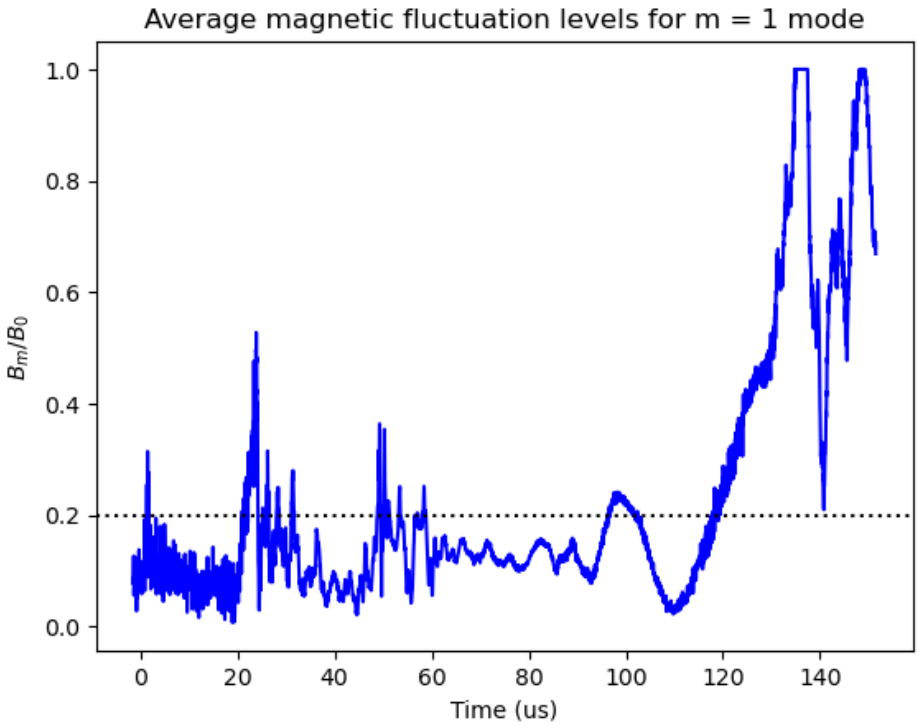

Figure 5.3: Average magnetic fluctuations for the m = 1 azimuthal mode measured at z = 20 cm during a day of plasma pulses. Value at or below 0.2 indicates a centered pinch at the axial location where the IDS data is taken. Data is from pulses 240506026-240506027 at Case III conditions.

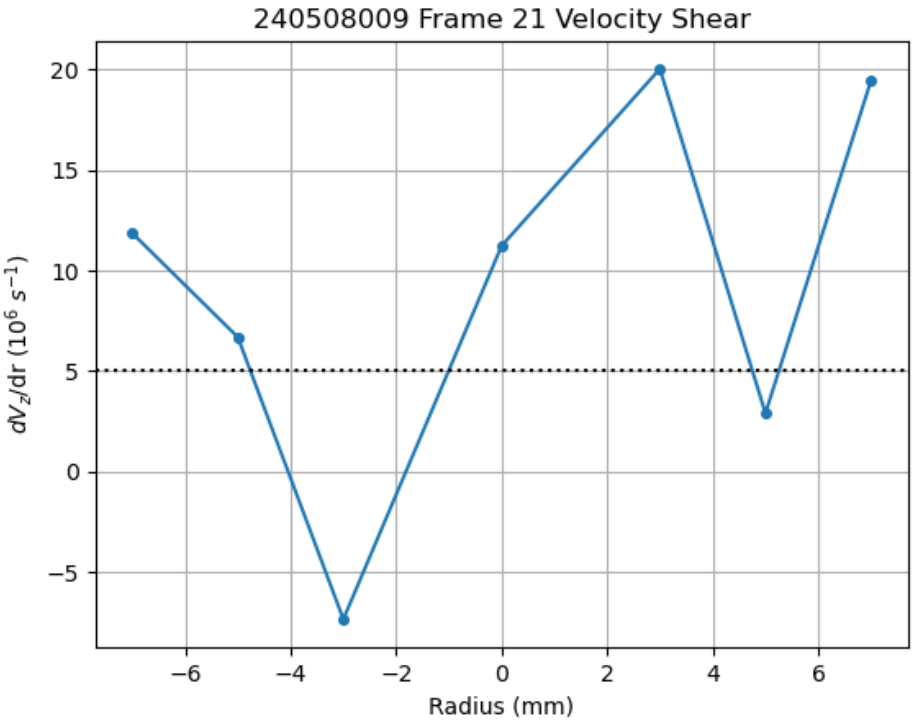

Figure 5.4: Radial shear velocity profile calculated from pulse 240506009 at 46.2 μs. Velocity shear on the edges is well above the threshold needed for sheared-flow stabilization shown with a dotted black line. Data is from a pulse at Case II conditions.

5.2 Past Results

Comparison to past time resolved IDS data for ZaP-HD collected on a different high speed camera shows similar magnitudes for velocity and temperature profiles. Velocity data collected in Ref [16] shows velocity peaks of 140 km/s when operating at Case II conditions. The sheared-flow profile is not seen, however the data is only from one pulse, so that could be down to the variability of each pulse. The amount of carbon impurities in the plasma is also greater now due to continued degradation of the graphite nose cone in the machine, so data was able to be collected over a broader time range with increased accuracy. The temperature profiles in Ref [16] show temperature peaks of 350 eV occurring after the quiescent period for similar run conditions. Late in the plasma pulse, data from this thesis also shows peaks in temperature after the quiescent period, but the data was thrown out due to bad fits. At later times in the pulse, the temperature chords exhibit more noise as the C III intensity lowers, which leads to artificial broadening and could account for a late peak in temperature. The stagnation in plasma velocity and jump in temperature were also not seen, however this jump takes place earlier in the plasma pulse than most of the past data. Sheared-flow on the original ZaP device exhibited a shear reversal halfway through the quiescent period which is not seen here. There is also no drop in velocity at the onset of quiescence, but the initial velocity magnitude before the drop off and the shear gradient are comparable [32].

5.2.1 Plasma Stagnation

Initially it was thought the higher velocities before the quiescent period could be caused by radial motion of the plasma during periods of high magnetic field fluctuations. Fig 5.1 shows a relatively well centered pinch starting as early as 30 μs, and absolute velocity profiles should account for radial contributions, so other possible explanations seemed more likely to cause this. The velocity and temperature profiles share characteristics with the upstream and downstream behaviors associated with a normal shock, so this is investigated. The current front of the snowplow moving

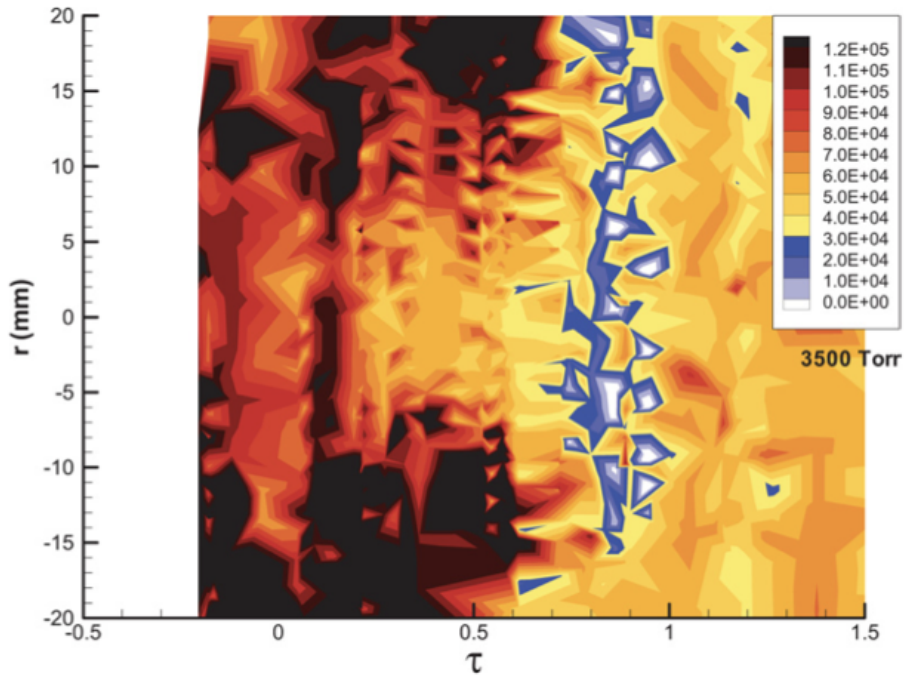

Figure 5.5: Contours of axial velocity in m/s as a function of radius at z = 0 for a normalized time, τ corresponding to a quiescent period of 42 to 79 μs. Sheared flow is evident in the quiescent period with a 'shear reversal' at $\tau = .5$ [32]

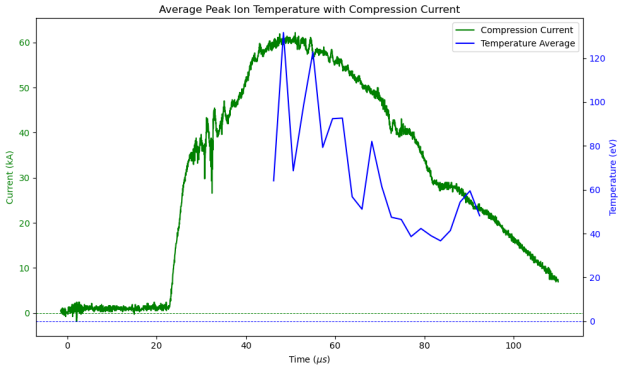

(a) Case I

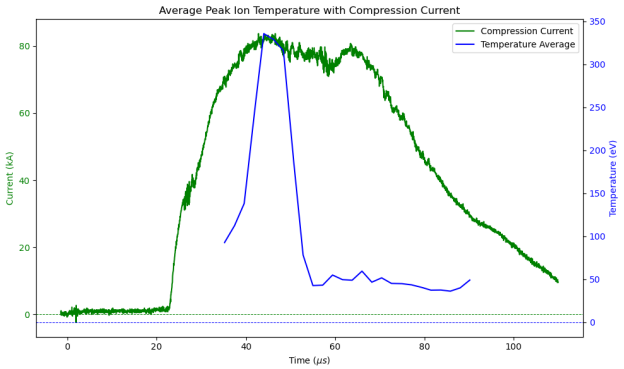

(b) Case II

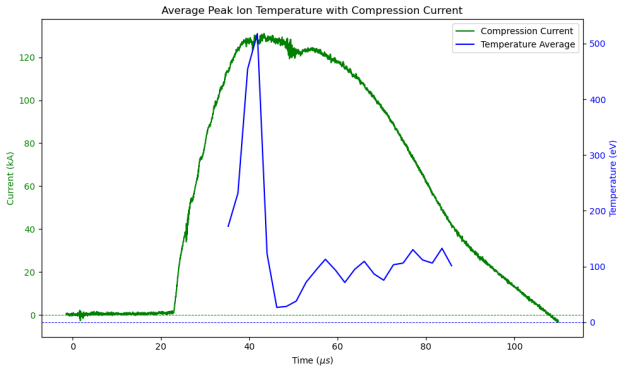

(c) Case III

Figure 5.6: Average temperature across all chords for each point in time is plotted with the compression current trace through time. a) is over Case I pulses and the current trace is from pulse 240508005. b) is over all Case II pulses from 240506 and 240508. d) is over Case III pulses 240506026-240506027.

through the acceleration region acts as a MHD shock, however this shock front dissipates within the assembly region and arrives much earlier in time than the $\approx 46\mu s$ that the discontinuity appears. Time was spent attempting to find evidence of the snowplow shock and possible deflagration that follows, but without access to acceleration region magnetic field data, no conclusions could be made on that topic. Past work has observed plasma reflecting off the end wall even with a spoked end wall when the plasma ram pressure is lower than the magnetic tension at the spokes [14; 33; 34].

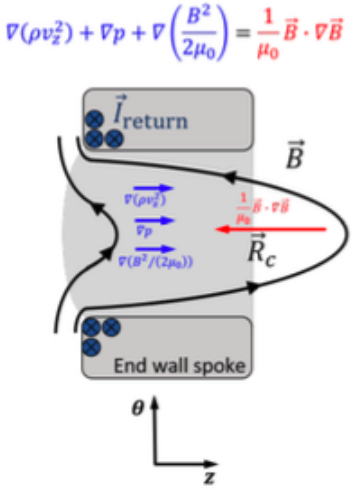

Figure 5.7: Force balance at current spoked end wall used on ZaP-HD. If the outward plasma ram pressure is not greater than the magnetic tension, plasma cannot demagnetize and enter the exhaust chamber. Even with the open holes, it can still act as a solid end wall and reflect plasma. [33; 34]

Magnetic field data from Case II and Case III operating conditions show a high current region propagating against the downstream direction of plasma flow. For Case I, the high current region affects magnetic field values at z = 40, but does not propagate further upstream most likely due to lower momentum at the lower voltage settings. This explains why IDS results from Cases II and III display features consistent with a normal shock and Case I does not. Though there is no IDS data from operating at 5 kV acceleration and 3 kV compression voltages, magnetic field data is collected to confirm the trend of less reflected plasma with lower input power. The reflected plasma

wave can be seen in Fig 5.8 when magnetic field magnitudes increase in an upstream propagating fashion. The feature associated with the additional magnetic flux due to the reflected plasma is more easily discerned in Fig 5.9, where the two lower voltage settings provide examples of data unaffected by plasma build up.

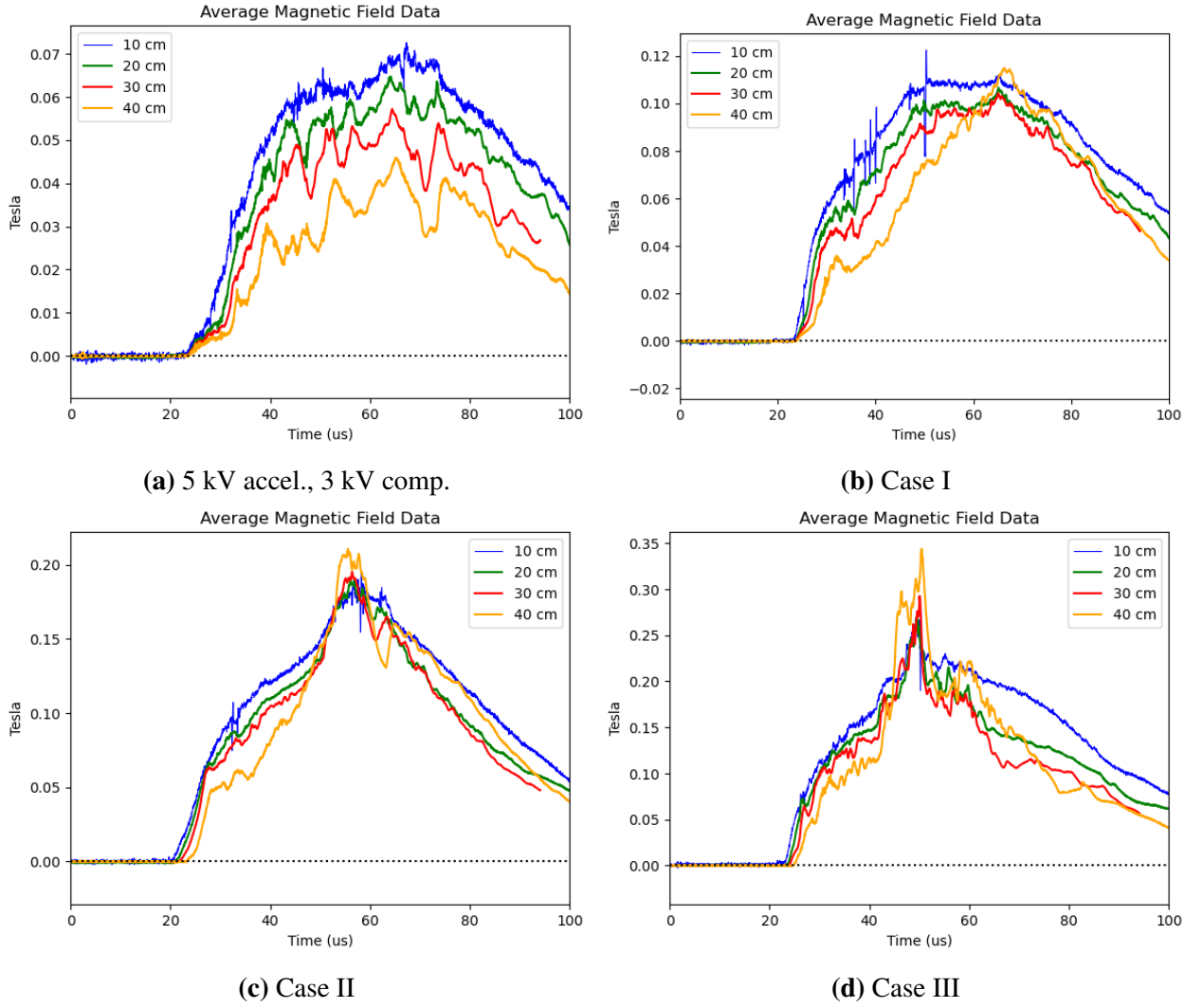

(a) 5 kV accel., 3 kV comp.

(b) Case I

(c) Case II

(d) Case III

Figure 5.8: Average magnetic field values at the outer electrode throughout time for 4 different axial locations. a) is the low voltage pulse average and data is from pulses 240424003, 240429003, 240501003, 240506003, 240508003. b) is for Case I conditions over pulses 240424004-240424007, 240508004-240508006. c) Case II conditions over pulses 240508007-240508020. d) Case III conditions over pulses 240506026-240506027.

Past work has successfully analyzed coaxial plasma accelerators as 1D systems with Rankine-

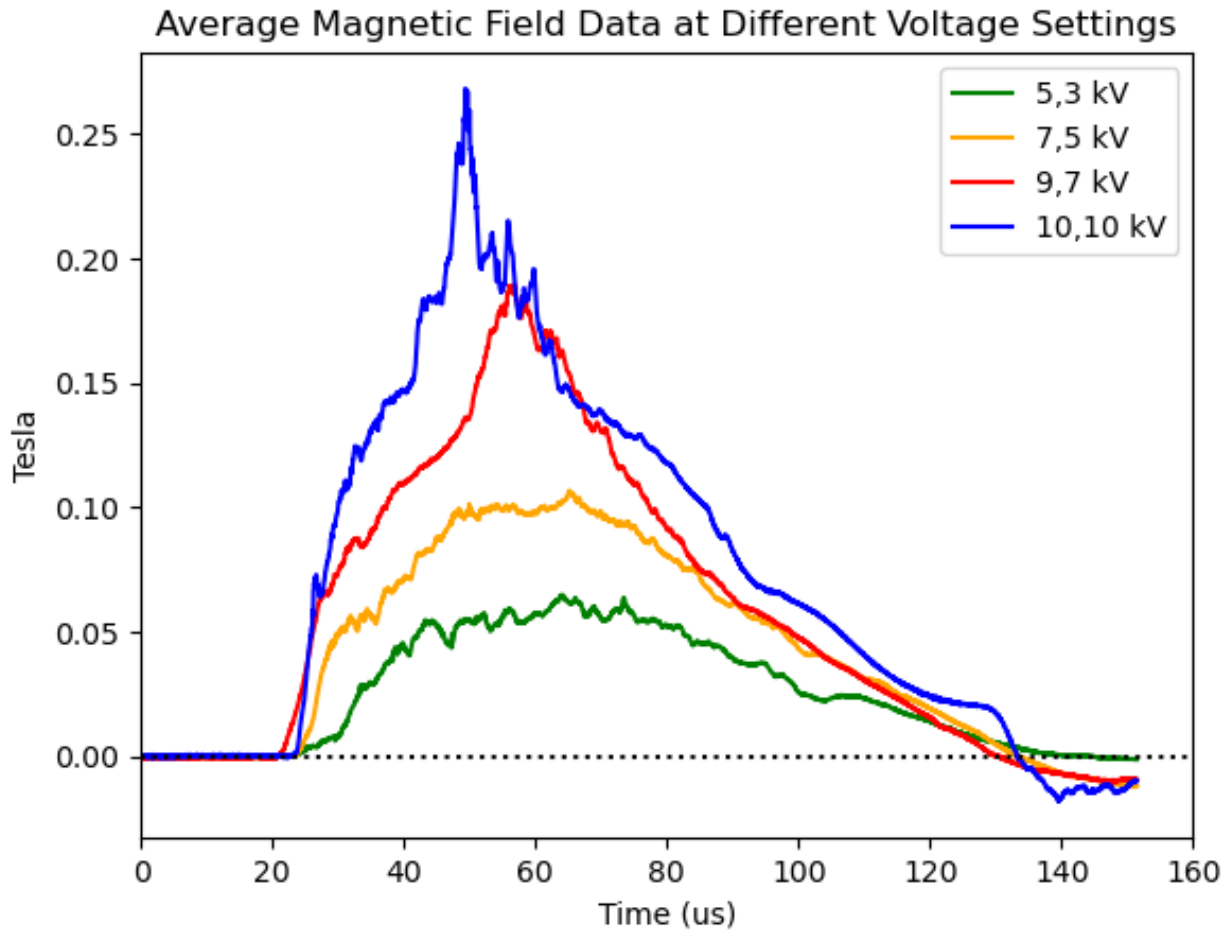

Figure 5.9: Azimuthal magnetic field data for multiple voltage settings at the same axial location of z = 20 is shown. The magnetic flux compression from the reflected plasma wave is featured in the two higher voltage settings, but lacks the energy to propagate to z = 20 at the lower voltage settings.

Hugoniot jump conditions applied to ideal MHD equations to model shockwaves [13] [35]. Plasma reflection was observed in other Z pinch experiments and also early coaxial accelerators [33] [36]. The wave is interpreted as a stagnation wave and treated as a shock in the wave frame of reference. The wave is traveling at a velocity v_w upstream, opposite of plasma flow, and a schematic of the shock in the shock reference frame is shown in Fig 5.10. Mass conservation across the shock gives a density relation

$$\frac{n_2}{n_1} = \frac{v_p + v_w}{v_w} \tag{5.1}$$

where n_1 and n_2 are the upstream and downstream number densities and v_p is the upstream plasma velocity. Assuming frozen-in flux conditions and a normal shock that is perpendicular to the magnetic field, the number density ratio is equivalent to the magnetic field ratio.

$$\frac{B_2}{B_1} = \frac{n_2}{n_1} \tag{5.2}$$

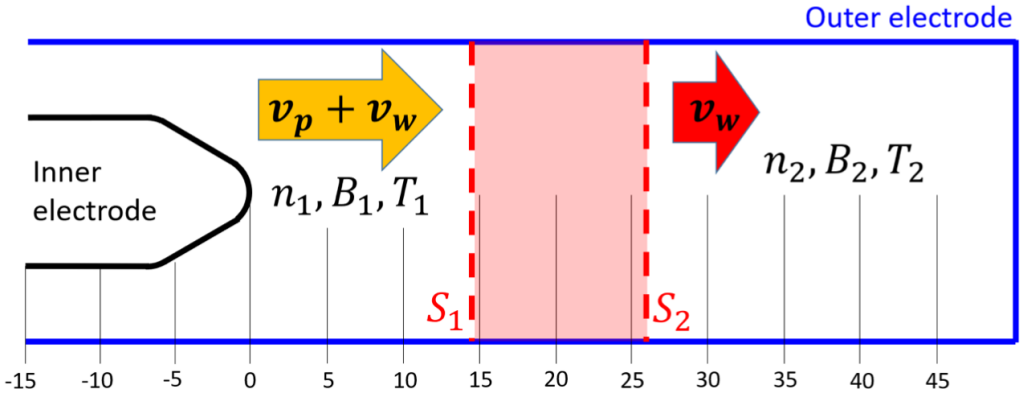

Figure 5.10: Jump conditions for the traveling stagnation wave in the wave reference frame. (1) corresponds to upstream conditions and (2) corresponds to downstream [33].

Solving the 1D ideal MHD conservation of mass, momentum, and energy equations leads to

the Rankine-Hugoniot jump condition for the shock

$$\frac{P_2^*}{P_1^*} = \frac{\frac{\gamma+1}{\gamma-1} - \frac{n_1}{n_2}}{(\frac{\gamma+1}{\gamma-1})\frac{n_1}{n_2} - 1} \tag{5.3}$$

where P^* is the sum of thermal and magnetic pressures and γ is the ratio of heat capacities and equals 5/3 for a monatomic gas such as hydrogen. Due to time constraints more work was not able to be done confirming the validity of the jump conditions, but Ref [33] shows a similar analysis done on the FuZE device. A quick calculation is done with $v_p \approx 140$ km/s and calculating $v_w \approx 110$ km/s using the propagation of the magnetic field perturbation upstream. From Eq. (5.1), the density ratio equals 2.27. Using $\frac{n_2}{n_1}$ in Eq. (5.3), a temperature jump condition of $\frac{T_2}{T_1} = 4.68$ is found. This is higher than the jump seen in the temperature profiles, however could be due to C III fully ionizing at temperatures that high. The dissipation of heat seen relatively quickly after the stagnation wave heats the plasma for Case II and III is an interesting feature and more work needs to be done to determine the exact cause. Carbon burnout is one possible explanation. As the stagnation wave heats the plasma, it could fully ionize all the C III, leaving only higher ionization levels of carbon at that location in the plasma. Using Fig 5.9 and comparing the two settings leading to reflected plasma at z = 20 with the other settings, the arrival of the stagnation wave can be estimated as the time when the magnetic field data departs from the expected trend seen on the green and yellow curves. This happens when the red and blue curves switches from concave down to concave up, which is $\approx$41 μs for Case III conditions and $\approx$46 μs. At higher voltages, higher speeds are expected, so the reflected plasma returns at an earlier time. The time resolved IDS results for Case II and III show agreement with the arrival time of the stagnation wave from magnetic field data.

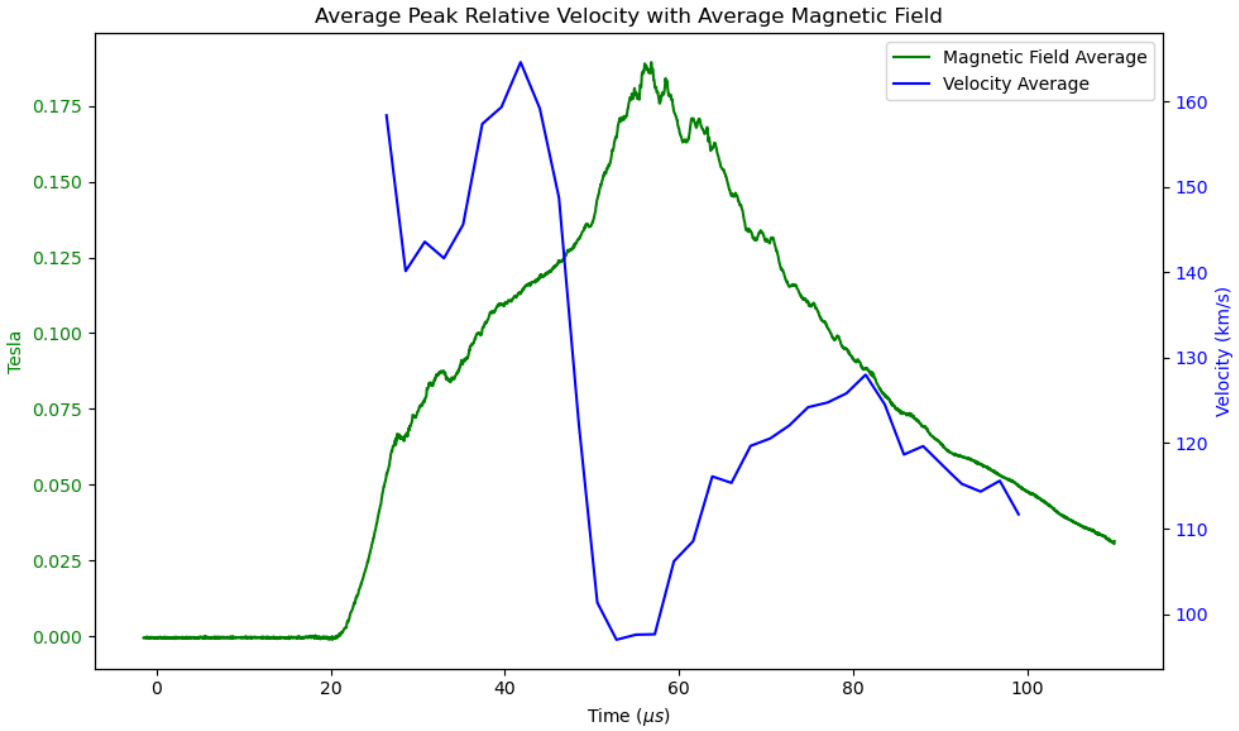

(a) Velocity and Magnetic Field

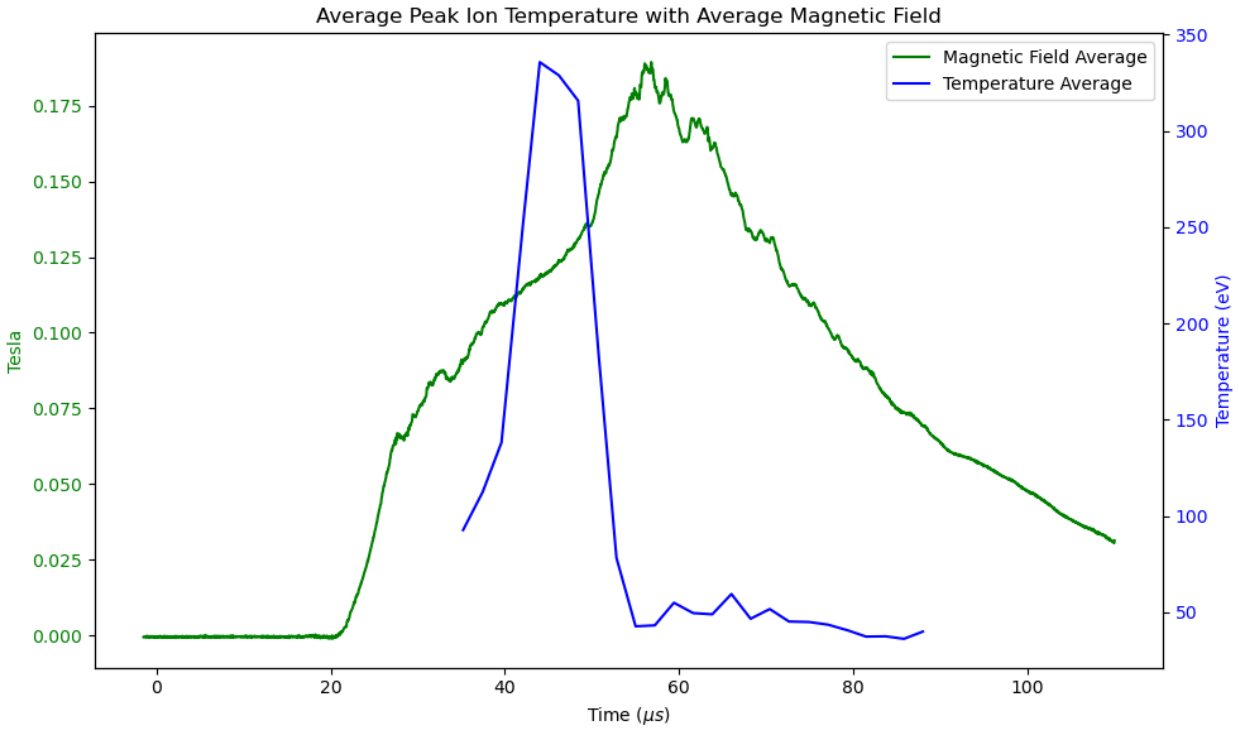

(b) Temperature and Magnetic Field

Figure 5.11: The temperature and velocity profiles through time are plotted with the magnetic field at z = 20. a) shows the peak velocity at each frame taken from the average relative ion velocity profile from all Case II pulses plotted with the average magnetic field at z = 20 from Case II pulses 240508007-240508020. b) is the peak ion temperature at each time period from the average ion temperature over all Case II pulses plotted with the average magnetic field at z = 20 from Case II pulses 240508007-240508020.

5.3 Propulsion Applications

Besides fusion applications, the Z pinch configuration shows promise as a form of pulsed plasma propulsion. ZaP-HD succeeds in accelerating fuel to high velocities in relatively short time periods. Plume characteristics for ZaP-HD differ from that of the assembly region, so IDS data from this paper cannot accurately show the behavior of plasma in the exhaust region of the device. Previous work shows plume dependence on the end wall configuration. Velocity in the exhaust region varies greatly depending on the amount of magnetic tension in opposition of the plasma ram pressure at the end wall electrode. The geometry of the end wall determines the force the plasma must overcome to flow into the exhaust region. ZaP-HD can operate without an end wall, allowing maximum flow through and thus higher plume velocities, but this comes at the cost of a less stable pinch [14]. For a hypothetical nuclear propulsion device, where fusion powers the spacecraft as well as provides thrust, the pinch stability is of utmost importance. Future work needs to be done with the oblique telescope looking at the exhaust chamber to find time resolved IDS data past the end wall. Since this thesis does not contain data past the end wall, quick calculations are done using the assembly region data collected and assuming a 100 % flow through for upper limit estimates on thrust and specific impulse. Exit velocity is found by the average ion relative velocity from 35.2 μs to 88.0 μs from Case I since there would be no stagnation wave with an open end wall geometry. To calculate thrust and specific impulse, an equivalent exit velocity is found to account for pressure thrust from the exhaust.

$$V_{eq} = V_e + \frac{(P_e - P_0)A_e}{\dot{m}} \tag{5.4}$$

For in space propulsion, the ambient pressure P_0 is 0 Pa. Mass flow rate, $\dot{m}$ is found assuming a number density of $10^{23} m^{-3}$ and hydrogen as the propellant. Assuming an ideal gas, the exhaust

pressure can be found.

$$P_e = nk_bT \tag{5.5}$$

$$F_T = \dot{m}V_{eq} \tag{5.6}$$

$$I_{sp} = \frac{V_{eq}}{g_0} \tag{5.7}$$

Making the assumption of a constant density from 35.2 μs to 88.0 μs, thrust can be plotted against time and a total impulse is found from finding the area under the curve.

$$I_{tot} = \int F_T dt \tag{5.8}$$

This gives another way to solve for specific impulse where

$$I_{sp} = \frac{I_{tot}}{mg_0} \tag{5.9}$$

which allows for a comparison between the two methods of calculation. Using the total impulse calculated from Fig 5.12 and Eq. (5.9) gives a specific impulse of 5.76×10^4 s and Eq. (5.7) leads to 6.04×10^4 s. This 4.75 % difference shows good agreement between the two methods. ZaP-HD is a pulsed device, so the total impulse calculated earlier is actually an impulse bit. To turn this per pulse impulse bit into an effective thrust, a pulse frequency needs to be assumed. A 10 Hz pulse rate leads to an effective thrust of 216 mN. Compared to previous thruster parameters calculated for ZaP-HD, a similar magnitude of specific impulse and thrust is found [14].

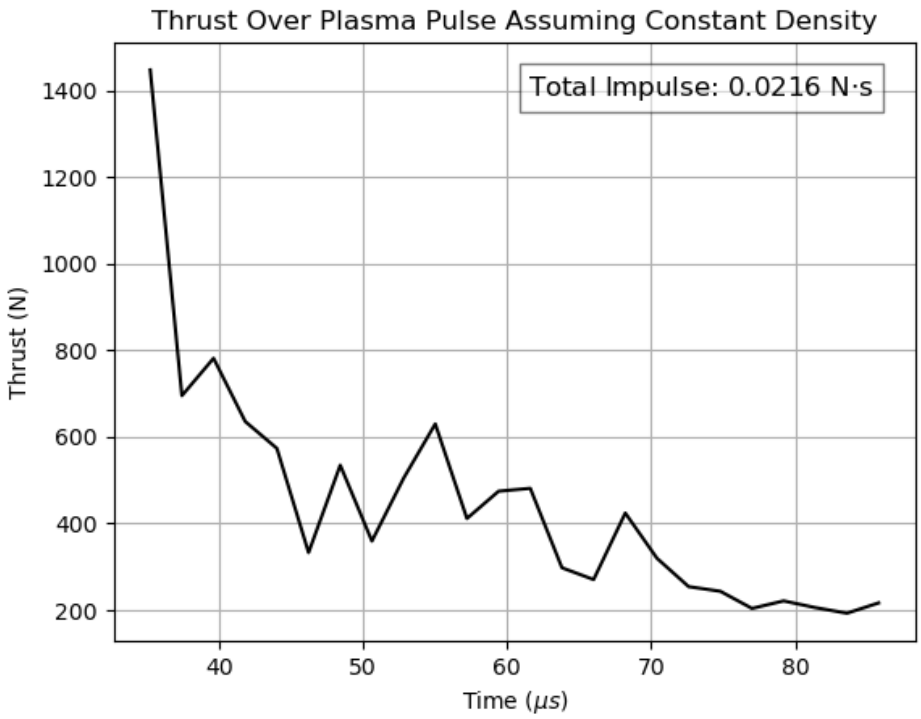

Figure 5.12: An average thrust profile for ZaP-HD operating under Case I conditions from pulses 240508004-240508006 assuming a constant density and 100 % flow through.

CHAPTER 6

CONCLUSION

Ion Doppler temperature and velocity measurements were successfully taken on the ZaP-HD device using a new spectroscopy setup allowing for time and space resolved data. Due to increased C III impurities in the plasma from the graphite nose cone, stronger signals were seen compared to past attempts at time-resolved IDS data. The Phantom camera also increased spatial resolution to a little over twice that of previous setups. Velocity profiles throughout the plasma lifetime give indications of a sheared plasma flow which increases stability. Temperature evolution shows a plasma with a high temperature core and lower temperature on its outer edges. IDS data shows evidence of reflected plasma causing magnetic flux compression in the plasma. One possible explanation of the results is a reflected plasma wave acts as an upstream propagating shock wave with jump conditions that can be found using 1D ideal MHD conservation equations. The reflected wave reaches further upstream at faster speeds with higher voltage settings. The arrival of a theorized stagnation wave is found using magnetic field measurements and corresponds to a drop in velocity and rise in temperature of the plasma as the shock crosses the axial location. A possible explanation for the fast drop in temperature is burn-through of C III, giving motivation for future C V measurements. The increased performance of the Phantom over past cameras could allow space and time resolved measurements of low intensity C V that were not previously possible.

Shear velocity is shown to be above the threshold needed to mitigate m = 1 instabilities in the plasma during quiescence in all three cases investigated. If not for the reflected plasma, velocity

and temperature would both increase with current and then fall off as current returns to 0. Data with the end wall off was not taken, but for future work, could ensure little to no plasma stagnation with temperature and velocity profiles in agreement with plasma current for all voltage settings.

CHAPTER 7

FUTURE WORK

This thesis was able to provide a method for space and time resolved ion Doppler spectroscopy data using a high speed camera that had not been used on ZaP-HD before. More work can now be done with this setup to better understand the plasma dynamics over the full time period and scale length of the pinch. More pulses with the Phantom should be conducted to provide statistical significance to measurements on ZaP-HD. A more rigorous error analysis, such as that performed on radially deconvolved spectra by Golingo and Shumlak, should be conducted to account for uncertainties in the measuring instruments [37]. Weak signals at lower voltages could be solved by doping the plasma with methane and more pulses could be taken at lower voltages to confirm the trends seen in this thesis. With more time a more rigorous examination of the Rankine-Hugoniot jump conditions could be done and compared with the IDS results for upstream and downstream parameters.

Other impurity ions of interest, such as carbon V, offer the prospect of looking at higher temperature plasma. Previous work on FuZE points to a pinch with high temperature C V emission coming from the core of the plasma, while the lower temperature C III resides mainly on the lower temperature outer shells [33]. Being able to capture the evolution and behavior of both carbon impurity ions over time and space in ZaP-HD with the Phantom could confirm those results and offer further insight into the flow profile. For applications into propulsion and shear-flow stabilization, once the magnetic field probes in the accelerator region are available for use, work could be done

characterizing the current sheet evolution from the accelerator region through the assembly region. Previous work on ZaP-HD and coaxial plasma accelerators has shown gas puff timing affects the acceleration mode. While snowplow mode compresses and heats the plasma more, deflagration could be more beneficial for propulsion purposes as it more efficiently converts magnetic energy into axial velocity and leads to less electrode erosion [13]. Magnetic field data from the accelerator region can show which mode ZaP-HD is operating in and IDS data for both modes could be compared. Velocity measurements could be taken with the end wall off and on with the 35 degree oblique scope aimed at the exhaust chamber to directly compared the time-resolved data with previous ZaP-HD plume velocity measurements.

BIBLIOGRAPHY

[1] P. Friedlingstein, M. O'sullivan, M.W. Jones, R.M. Andrew, L. Gregor, J. Hauck, C. Le Quéré, I.T. Luijkx, A. Olsen, G.P. Peters, et al. Global carbon budget 2022. *Earth system science data*, 14(11):4811–4900, 2022.

[2] J.D. Lawson. Some criteria for a power producing thermonuclear reactor. *Proceedings of the physical society. Section B*, 70(1):6, 1957.

[3] S.E. Wurzel and S.C. Hsu. Progress toward fusion energy breakeven and gain as measured against the lawson criterion. *Physics of Plasmas*, 29(6), 2022.

[4] U. Shumlak, E.T. Meier, and B.J. Levitt. Fusion gain and triple product for the sheared-flow-stabilized z pinch. *Fusion Science and Technology*, 80(1):1–16, 2024.

[5] F.F. Chen. *Introduction to Plasma Physics and Controlled Fusion*. Springer, 2016.

[6] C.W. Hartman, D.Y. Cheng, G.E. Cooper, J.L. Eddleman, and R.H. Munger. High density fusion and the z-pinch. Technical report, California Univ., Livermore (USA). Lawrence Livermore Lab., 1974.

[7] R.L. Hagenson, A.S. Tai, R.A. Krakowski, and R.W. Moses. The dense z-pinch (dzp) as a fusion power reactor: Preliminary scaling calculations and systems energy balance. *Nuclear Fusion*, 21(11):1315, 1981.

[8] J. Sethian. The quest for a z-pinch based fusion energy source—a historical perspective. In *AIP Conference Proceedings CONF-9705120*, volume 409, pages 3–10. American Institute of Physics, 1997.

[9] T.G. Cowling. Magnetohydrodynamics. *Reports on Progress in Physics*, 25(1):244, 1962.

[10] U. Shumlak, R. Lilly, C. Adams, R. Golingo, S. Jackson, S. Knecht, and B. Nelson. Advanced space propulsion based on the flow-stabilized z-pinch fusion concept. In *42nd AIAA/ASME/SAE/ASEE Joint Propulsion Conference & Exhibit*, page 4805, 2006.

[11] R.P. Golingo, U. Shumlak, and B.A. Nelson. Formation of a sheared flow z pinch. *Physics of Plasmas*, 12(6), 2005.

[12] T.D. Arber and D.F. Howell. The effect of sheared axial flow on the linear stability of the z-pinch. *Physics of Plasmas*, 3(2):554–560, 1996.

[13] D.Y. Cheng. Plasma deflagration and the properties of a coaxial plasma deflagration gun. *Nuclear Fusion*, 10(3):305, 1970.

[14] J. Smythe. Electrode geometry effects on plume characteristics and thruster performance of zap-hd. Master's thesis, University of Washington, 2023.

[15] B. Diamond. Spatio-temporally resolved magnetic field measurements in the zap-hd flow z-pinch device using zeeman splitting. Master's thesis, University of Washington, 2022.

[16] E. Forbes. *Diagnostic Development and Plasma-Material Interaction Studies on the ZaP-HD Device*. PhD thesis, University of Washington, 2020.

[17] E.G. Forbes and U Shumlak. Spatio-temporal ion temperature and velocity measurements in a z pinch using fast-framing spectroscopy. *Review of Scientific Instruments*, 91(8), 2020.

[18] A. Khairi. Graphite electrode characterization on the zap-hd sheared-flow-stabilized z-pinch device. Master's thesis, University of Washington, 2021.

[19] GCSE Physics. The doppler effect. `https://online-learning-college.com/knowledge-hub/gcses/gcse-physics-help/doppler-effect/`, 2022.

[20] H.R. Griem. *Principles of Plasma Spectroscopy*. Cambridge University Press, 1997.

[21] J.R. Roberts. Optical emission spectroscopy on the gaseous electronics conference rf reference cell. *Journal of research of the National Institute of Standards and Technology*, 100(4): 353, 1995.

[22] I.H. Hutchinson. *Principles of Plasma Diagnostics*. Cambridge University Press, 1987.

[23] M.P. Ross and U. Shumlak. Digital holographic interferometry employing fresnel transform reconstruction for the study of flow shear stabilized z-pinch plasmas. *Review of Scientific Instruments*, 87(10), 2016.

[24] M.P. Ross. *Exploring plasma stability and confinement with high resolution density measurements on the ZaP-HD Flow Z-Pinch*. PhD thesis, University of Washington, 2016.

[25] R.P. Golingo and U. Shumlak. Spatial deconvolution technique to obtain velocity profiles from chord integrated spectra. *Review of scientific instruments*, 74(4):2332–2337, 2003.

[26] Y. Bai, J. Bajaj, J.W. Beletic, M.C Farris, A. Joshi, S. Lauxtermann, A. Petersen, and G. Williams. Teledyne imaging sensors: silicon cmos imaging technologies for x-ray, uv, visible, and near infrared. In *High energy, optical, and infrared detectors for astronomy III*, volume 7021, pages 29–44. SPIE, 2008.

[27] R. Hain, C.J Kähler, and C. Tropea. Comparison of ccd, cmos and intensified cameras. *Experiments in fluids*, 42:403–411, 2007.

[28] L.G. Alemany, C.M James, T.G Cullen, and Y. Liu. Investigation of visible to near-infrared high-speed cameras for thermography in hypersonic testing. *Experiments in Fluids*, 64(12): 189, 2023.

[29] Rongland Ltd. Image intensifier tubes - how it works. `https://rongland.co.uk/blogs/news/image-intensifier-tubes-how-it-works`, 2023.

[30] S.F. Jacobs. How a diffraction grating works. https://wp.optics.arizona.edu/sfjacobs/wp-content/uploads/sites/47/2016/06/DiffractionGratings.pdf, 1996.

[31] D.D. Hartog and R.P. Golingo. Telecentric viewing system for light collection from az-pinch plasma. *Review of Scientific Instruments*, 72(4):2224–2225, 2001.

[32] U. Shumlak, C.S. Adams, J.M. Blakely, B.J. Chan, R.P. Golingo, S.D. Knecht, B.A. Nelson, R.J. Oberto, M.R. Sybouts, and G.V. Vogman. Equilibrium, flow shear and stability measurements in the z-pinch. *Nuclear fusion*, 49(7):075039, 2009.

[33] E.L. Claveau. *Axial Evolution of a Sheared-Flow-Stabilized Z Pinch*. PhD thesis, University of Washington, 2020.

[34] E.L. Claveau, U. Shumlak, B.A. Nelson, E.G. Forbes, A.D. Stepanov, T.R. Weber, Y. Zhang, and H.S. McLean. Plasma exhaust in a sheared-flow-stabilized z pinch. *Physics of Plasmas*, 27(9), 2020.

[35] K.T. Loebner, T.C. Underwood, and M.A. Cappelli. Evidence of branching phenomena in current-driven ionization waves. *Physical review letters*, 115(17):175001, 2015.

[36] C.T. Chang. Shock wave phenomena in coaxial plasma guns. *The Physics of Fluids*, 4(9): 1085–1096, 1961.

[37] R.P. Golingo, U. Shumlak, and D.J. Hartog. Note: Zeeman splitting measurements in a high-temperature plasma. *Review of Scientific Instruments*, 81(12), 2010.

CHAPTER A

APPENDIX A

A.1 Calibration and Operation of Fast Framing Spectroscopy with the Phantom T2410

This section details how to align and calibrate the Phantom high speed camera in conjunction with the SIL3 image intensifier for the spectroscopic measurements taken in this thesis.

A.1.1 Optics Setup and Alignment

The necessary items to begin with are the Phantom camera, the SIL3 image intensifier, a Samyang 85mm f/1.4 aspherical IF lens, and of course the spectrometer itself, which will already be in position on the optics table.

1. Attach the lens to the end of the SIL3 without the shutter by using the thread on the end of the lens

2. Once the lens is attached, it can be mounted to the Phantom. The lens can also be mounted to the Phantom and then threaded to the SIL3, but it was found to be a more difficult process.

3. In order to run at high frame rate while still observing all 20 chords from the spectrometer the Phantom needs to be on its side, so a base made out of wood blocks was used to support the camera while also not blocking the airflow from the cooling fans. A more robust structure could

be made that threads into the optics table for an easier and more repeatable setup.

4. Once the camera is successfully married to the intensifier and both are in position on the optics table, the user can move on to alignment.

5. Turn on the spectrometer, camera, and intensifier and a cadmium pen-lamp.

6. Insert the joined end of the split fiber cable into the spectrometer and make sure the entrance slit is $\approx 20\mu m$. Ensure the split ends of the cable are pointed at the cadmium lamp.

7. In the control room use one of the computers to open Acton Research Corporation SpectraPro Monochromator Control Software and set the grating to 3600 g/mm and set the wavelength of interest to 228.8 nm. Using the Kirana laptop open the SIL3 software and use the focus button to activate the intensifier.

8. On the Phantom laptop, open the Phantom Camera Control software, select camera 30599 and make sure it is in live mode.

9. At this point adjust the exposure time on the SIL3 and Phantom software until the 228.8 nm spectral line is visible.

10. Once visible, alignment can be done by putting the intensifier as flush with the spectrometer entrance as possible. Additional optics can be used to ensure the focal planes are aligned, but that was not done for this thesis. Once flush with the spectrometer, manual adjustment must be done until the spectral line is centered.

A.1.2 Calibration

Now that the camera, intensifier, and spectrometer are setup and aligned, a calibration must be done.

1. Leaving the setup as in the previous section, the only change is on the Monochromator Control Software, set the wavelength of interest to 227.5 nm. This ensures that both the 228.8 nm and 226.5 nm lines will be visible on the same frame. Some adjustment might need to be done with the exposure times and gain of the intensifier to see both lines.

2. Save a frame that contains both lines. This can be done using the capture option on the Phantom software. After captured, look through all the frames and save one where both lines are visible as a '.tif'.

3. With this '.tif' file a pixel space to wavelength space linear mapping can then be completed.

A.1.3 Capturing Spectra Over a Plasma Pulse

The intensifier and camera need to be synced in order to ensure that each phosphor rise and decay corresponds to a single frame. This can be done a few ways, but the steps used for this thesis are outlined.

1. Ensure the Phantom is in an external sync mode with a 2.22 μs delay.

2. Connect a BNC from the SIL3 AUX OUT port to the Phantom FSYNC port.

3. Connect a trigger to the SIL3 trigger input.

4. On the intensifier control software set a 1.22 μs exposure with $1\mu s$ separation and a 55 ns delay. These were the most repeatable settings that also led to a maximum number of frames per pulse.

5. Before each pulse arm the intensifier using the SIL3 software

6. After arming the intensifier click the 'Capture' button on the Phantom software. After that the 'Trigger' button must be clicked as well or it will not recognize the incoming signal from the intensifier.

7. Once the pulse is over, save the frames as individual '.tif' files for analysis.

8. Repeat steps 5-7 for every pulse.

If other settings are wanted, use an oscilloscope to ensure that the phosphor rise and decay are in sync with the camera shutter opening and closing. Use a split BNC to have one BNC from SIL3 AUX OUT to Phantom FSYNC and another from the AUX OUT to the oscilloscope. Another BNC from input 3 on the Phantom to the oscilloscope shows the shutter open and close signal.